



Contents lists available at ScienceDirect

# Medical Image Analysis

journal homepage: [www.elsevier.com/locate/media](http://www.elsevier.com/locate/media)

## Diffeomorphic metric mapping and probabilistic atlas generation of hybrid diffusion imaging based on BFOR signal basis



Jia Du<sup>a</sup>, A. Pasha Hosseinbor<sup>b,c</sup>, Moo K. Chung<sup>c,d</sup>, Barbara B. Bendlin<sup>e</sup>, Gaurav Suryawanshi<sup>c</sup>, Andrew L. Alexander<sup>b,c</sup>, Anqi Qiu<sup>a,f,g,\*</sup>

<sup>a</sup> Department of Biomedical Engineering, National University of Singapore, Singapore

<sup>b</sup> Department of Medical Physics, University of Wisconsin-Madison, USA

<sup>c</sup> Waisman Laboratory for Brain Imaging and Behavior, University of Wisconsin-Madison, USA

<sup>d</sup> Biostatistics and Medical Informatics, University of Wisconsin-Madison, USA

<sup>e</sup> Department of Medicine, University of Wisconsin-Madison, USA

<sup>f</sup> Singapore Institute for Clinical Sciences, Agency for Science, Technology and Research, Singapore

<sup>g</sup> Clinical Imaging Research Center, National University of Singapore, Singapore

### ARTICLE INFO

#### Article history:

Received 23 October 2013

Received in revised form 12 May 2014

Accepted 24 May 2014

Available online 11 June 2014

#### Keywords:

Hybrid diffusion imaging (HYDI)

Large deformation diffeomorphic metric mapping (LDDMM)

Bessel Fourier orientation reconstruction (BFOR) signal basis

Bayesian estimation

The white matter atlas

### ABSTRACT

We first propose a large deformation diffeomorphic metric mapping algorithm to align multiple  $b$ -value diffusion weighted imaging (mDWI) data, specifically acquired via hybrid diffusion imaging (HYDI). We denote this algorithm as LDDMM-HYDI. We then propose a Bayesian probabilistic model for estimating the white matter atlas from HYDIs. We adopt the work given in Hosseinbor et al. (2013) and represent the  $q$ -space diffusion signal with the Bessel Fourier orientation reconstruction (BFOR) signal basis. The BFOR framework provides the representation of mDWI in the  $q$ -space and the analytic form of the ensemble average propagator (EAP) reconstruction, as well as reduces memory requirement. In addition, since the BFOR signal basis is orthonormal, the  $L^2$  norm that quantifies the differences in the  $q$ -space signals of any two mDWI datasets can be easily computed as the sum of the squared differences in the BFOR expansion coefficients. In this work, we show that the reorientation of the  $q$ -space signal due to spatial transformation can be easily defined on the BFOR signal basis. We incorporate the BFOR signal basis into the LDDMM framework and derive the gradient descent algorithm for LDDMM-HYDI with explicit orientation optimization. Additionally, we extend the previous Bayesian atlas estimation framework for scalar-valued images to HYDIs and derive the expectation-maximization algorithm for solving the HYDI atlas estimation problem. Using real HYDI datasets, we show that the Bayesian model generates the white matter atlas with anatomical details. Moreover, we show that it is important to consider the variation of mDWI reorientation due to a small change in diffeomorphic transformation in the LDDMM-HYDI optimization and to incorporate the full information of HYDI for aligning mDWI. Finally, we show that the LDDMM-HYDI outperforms the LDDMM algorithm with diffusion tensors generated from each shell of HYDI.

© 2014 The Authors. Published by Elsevier B.V. This is an open access article under the CC BY-NC-ND license (<http://creativecommons.org/licenses/by-nc-nd/3.0/>).

### 1. Introduction

Diffusion-weighted MRI methods are promising tools for characterizing tissue microstructure. While diffusion tensor imaging (DTI) and high angular resolution diffusion imaging (HARDI) methods are widely used methods, they do not provide a complete description of the diffusion distribution. In order to more accurately reconstruct the ensemble average propagator (EAP), a

thorough the sampling of the  $q$ -space is needed, which requires multiple  $b$ -value diffusion weighted imaging (mDWI). The EAP estimation using mDWI better characterizes more complex neural fiber geometries and non-Gaussian diffusion behavior when compared to single  $b$ -value techniques (Wu and Alexander, 2007). Recently, new  $q$ -space imaging techniques, diffusion spectrum imaging (DSI) (Wedeen et al., 2005) and hybrid diffusion imaging (HYDI) (Wu and Alexander, 2007) have been developed for estimating the EAP. HYDI is a mDWI technique that samples the diffusion signal along concentric spherical shells in the  $q$ -space. The number of encoding directions increases with each shell to increase the angular resolution with the level of diffusion weighting. Originally, HYDI employed the fast Fourier transform (FFT) to

\* Corresponding author. Address: Department of Biomedical Engineering, National University of Singapore, 9 Engineering Drive 1, Block EA 03-12, Singapore 117576, Singapore. Tel.: +65 6516 7002; fax: +65 6872 3069.

E-mail address: [bieqa@nus.edu.sg](mailto:bieqa@nus.edu.sg) (A. Qiu).

reconstruct the EAP. However, the recent advent of analytical EAP reconstruction schemes, which obtain closed-form expressions of the EAP, obviate the use of the FFT in HYDI. Such reconstruction schemes include diffusion propagator imaging (DPI) (Descoteaux et al., 2011), simple harmonic oscillator based reconstruction and estimation (SHORE) (Ozarslan et al., 2008), spherical polar Fourier imaging (SPFI) (Cheng et al., 2010; Assemlal et al., 2009). One recent technique successfully validated on HYDI datasets is Bessel Fourier orientation reconstruction (BFOR) (Hosseinbor et al., 2013). While mDWI techniques like HYDI have not been widely used, the new human connectome project (Essen et al., 2013) and spin-off projects will likely significantly increase the application. However, there is a lack of fundamental image analysis tools for mDWI and EAP maps, such as registration and atlas generation, that can fully utilize their information.

In the last decades, researchers have spent great efforts on developing registration algorithms to align diffusion tensors derived from DTI and orientation distribution functions (ODFs) derived from HARDI (e.g., Alexander et al. (2001), Raffelt et al. (2011), Du et al. (2012)). However, registration algorithms directly based on DWIs are few. The direct alignment of DWIs in the  $q$ -space utilizes the full diffusion information, is independent of the choice of diffusion models and their reconstruction algorithms (e.g., tensor), and unifies the transformation to align the local diffusion profiles defined at each voxel of two brains (Dhollander et al., 2010; Yap and Shen, 2012; Zhang et al., 2012). Dhollander et al. (2010) developed an algorithm that transforms the diffusion signals on a single shell of the  $q$ -space and preserves anisotropic as well as isotropic volume fractions. Yap and Shen (2012) proposed to decompose the diffusion signals on a single shell of the  $q$ -space into a series of weighted diffusion basis functions, reorient these functions independently based on a local affine transformation, and then recombine the reoriented functions to obtain the final transformed diffusion signals. This approach provides the representation of the diffusion signals and also explicitly models the isotropic component of the diffusion signals to avoid undesirable artifacts during the local affine transformation. Zhang et al. (2012) developed a diffeomorphic registration algorithm for aligning diffusion signals on a single shell of the  $q$ -space.

Only recently, Dhollander et al. (2011) aligned DWIs on multiple shells of the  $q$ -space by first estimating transformation using a multi-channel diffeomorphic mapping algorithm, in which generalized fractional anisotropy (GFA) images computed from each shell were used as mapping objects, and then applying the transformation to DWIs on each shell using the DWI reorientation method given in Dhollander et al. (2010). This approach neglected possible influences of the DWI reorientation on the optimization of the spatial transformation. Hsu et al. (2012) generalized the large deformation diffeomorphic metric image mapping algorithm (Beg et al., 2005) to DWIs on multiple shells of the  $q$ -space and considered the image domain and the  $q$ -space as the domain where the diffeomorphic transformation is applied to. The authors claimed that the reorientation of DWIs is no longer needed because the transformation also incorporates the deformation due to the shape differences in the diffusion profiles in the  $q$ -space. It is a robust registration approach with the explicit consideration of the large deformation in both the image domain and  $q$ -space. However, its computational complexity and memory requirement are high.

While limited research has been done for aligning the HYDI images, efforts on the white matter atlas from HYDI is even less. Only recently, Dhollander et al. (2011) employed their multi-channel diffeomorphic matching algorithm to generate the atlas from multiple HYDI datasets. To our best knowledge, there is no probabilistic atlas generation approach for HYDI.

In this paper, we propose a large deformation diffeomorphic metric mapping (LDDMM) algorithm to align HYDI datasets,

denoted as LDDMM-HYDI, and then develop a Bayesian probabilistic estimation framework for generating the HYDI atlas. In particular, we adopt the Bessel Fourier orientation reconstruction (BFOR) framework in representing the  $q$ -space signal (Hosseinbor et al., 2013). Unlike the diffeomorphic mapping of mDWIs in Hsu et al. (2012), the BFOR signal basis provides the representation of the  $q$ -space signal and the analytic form of the EAP reconstruction, as well as reduces memory requirement. In addition, since the BFOR signal basis is orthonormal, the  $L^2$  norm that quantifies the differences in the  $q$ -space signals can be easily computed as the sum of the squared differences in the BFOR expansion coefficients. In this work, we will show that the reorientation of the  $q$ -space signal due to spatial transformation can be easily defined on the BFOR signal basis. Unlike the work in Dhollander et al. (2011), we will incorporate the BFOR signal basis into the LDDMM framework and derive the gradient descent algorithm for solving the LDDMM-HYDI variational problem with explicit orientation optimization. Even though the LDDMM-HYDI algorithm is largely based on our previous work (Du et al., 2013), in this paper we further develop a Bayesian probabilistic model to estimate the brain white matter atlas from the  $q$ -space. This probabilistic model is the extension of the previous Bayesian atlas estimation for scalar-based intensity images (Ma et al., 2008). With the aids of the BFOR representation and reorientation of mDWIs introduced in this work, we show that it is feasible to adopt the previous Bayesian atlas estimation model for scalar-valued images (Ma et al., 2008) to HYDI. Nevertheless, the HYDI data has much higher dimensionality than the scalar image used in Ma et al. (2008). Moreover, the HYDI alignment requires the reorientation of the diffusion signals, while the scalar image alignment does not. Hence, we show that the extension of the Bayesian scalar image atlas generation in (Ma et al., 2008) to the HYDI data is not straightforward. In this paper, we thus reformulate the Bayesian atlas generation model for HYDI under the LDDMM framework and derive the expectation-maximization algorithm to optimize the HYDI atlas based on a set of HYDI data. As shown below, the main contributions of this paper are:

1. to seek large deformation for aligning HYDI datasets based on the BFOR representation of mDWI.
2. to derive the rotation-based reorientation of the  $q$ -space signal via the BFOR signal basis. This is equivalent to applying Wigner matrix to the BFOR expansion coefficients, where Wigner matrix can be easily constructed by the rotation matrix (see Section 3.1).
3. to derive the gradient descent algorithm for the LDDMM-HYDI variational problem with the explicit orientation optimization. In particular, we provide a computationally efficient method for calculating the variation of Wigner matrix due to the small variation of the diffeomorphic transformation (see Section 3.4).
4. to show that the LDDMM-HYDI gradient descent algorithm does not involve the calculation of the BFOR signal bases and hence avoids the discretization in the  $q$ -space.
5. to propose a Bayesian estimation model for the  $q$ -space signals represented via the BFOR signal basis and derive an expectation-maximization algorithm for solving it (see Section 4).
6. to validate the mapping accuracy of the LDDMM-HYDI algorithm and compare our approach with the LDDMM algorithm incorporating multiple diffusion tensors derived from each shell of the  $q$ -space. This has not been shown in our previous work (Du et al., 2013).

## 2. Review: BFOR signal basis

In this paper, we employ the BFOR signal basis to represent the  $q$ -space diffusion signal according to the work in Hosseinbor et al. (2013). The diffusion signal is assumed to satisfy Laplace's equa-

tion. The BFOR basis is derived based on the heat equation, a generalization of Laplace's equation and hence naturally incorporates water diffusion processes. In addition, the BFOR signal basis is orthonormal, which leads to the simple computation on the norm of the diffusion signals as shown below. Furthermore, the BFOR signal basis gives the analytic solution for the EAP as shown in Hosseinbor et al. (2013), which facilitates the registration of the EAP data via aligning the BFOR coefficients defined in the  $q$ -space. In the BFOR framework, the  $q$ -space diffusion signal,  $S(\mathbf{x}, \mathbf{q})$ , can be represented as

$$S(\mathbf{x}, \mathbf{q}) = \sum_{n=1}^{N_b} \sum_{j=1}^{N_y} c_{nj}(\mathbf{x}) \Psi_{nj}(\mathbf{q}), \quad (1)$$

where  $\mathbf{x}$  and  $\mathbf{q}$  respectively denote the image domain and  $q$ -space.  $\Psi_{nj}(\mathbf{q})$  is the  $nj$ -th BFOR signal basis with its corresponding coefficient,  $c_{nj}(\mathbf{x})$ , at  $\mathbf{x}$ .  $\Psi_{nj}(\mathbf{q})$  is given as

$$\Psi_{nj}(\mathbf{q}) = \frac{2\sqrt{\alpha_{nl(j)}}}{\sqrt{\pi\tau^3 J_{l(j)+3/2}(\alpha_{nl(j)})}} j_{l(j)} \left( \frac{\alpha_{nl(j)} |\mathbf{q}|}{\tau} \right) Y_j \left( \frac{\mathbf{q}}{|\mathbf{q}|} \right). \quad (2)$$

Here,  $\alpha_{nl}$  is the  $n$ th root of the  $l$ th order spherical Bessel (SB) function of the first kind  $j_l$ , then the eigenvalues are found to be  $-\lambda_{nl} = -\frac{\alpha_{nl}^2}{\tau^2}$ .  $\tau$  is the radial distance in  $q$ -space at which the Bessel function goes to zero. Note that for  $l=0$ , the roots are simply  $\alpha_{n0} = n\pi$ .  $Y_j$  are the modified real and symmetric spherical harmonics (SH) bases as given in Descoteaux et al. (2006).  $J_{l(j)+3/2}(\cdot)$  is the Bessel function of the first kind.  $N_y = \frac{(L+1)(L+2)}{2}$  is the number of terms in the modified SH bases of truncation order  $L$ , while  $N_b$  is the truncation order of radial basis.

Using the fact that the BFOR signal basis is orthonormal, the  $L^2$ -norm of  $S(\mathbf{x}, \mathbf{q})$  can be easily written as

$$\begin{aligned} \|S(\mathbf{x}, \mathbf{q})\|_2 &= \sqrt{\int_{\mathbf{x} \in \mathbb{R}^3} \int_{\mathbf{q} \in \mathbb{R}^3} S^2(\mathbf{x}, \mathbf{q}) d\mathbf{q} d\mathbf{x}} \\ &= \sqrt{\int_{\mathbf{x} \in \mathbb{R}^3} \sum_{n=1}^{N_b} \sum_{j=1}^{N_y} c_{nj}^2(\mathbf{x}) d\mathbf{x}}. \end{aligned} \quad (3)$$

### 3. Large deformation diffeomorphic metric mapping for HYDI

#### 3.1. Rotation-based reorientation of $S(\mathbf{x}, \mathbf{q})$

We now discuss the reorientation of  $S(\mathbf{x}, \mathbf{q})$  when a rotation transformation,  $R$ , is applied. We assume that the diffusion profile in each shell of the  $q$ -space remains in the same shell after the reorientation. However, its angular profile in each shell of the  $q$ -space is transformed according to the rotation transformation. Hence, we define

$$RS(\mathbf{x}, \mathbf{q}) = S(\mathbf{x}, R^{-1}\mathbf{q}).$$

In order to characterize  $RS(\mathbf{x}, \mathbf{q})$  based on the BFOR signal basis given in Eq. (1), we separate the angular and radial coordinates such that

$$RS(\mathbf{x}, \mathbf{q}) = S\left(\mathbf{x}, |\mathbf{q}|R^{-1}\frac{\mathbf{q}}{|\mathbf{q}|}\right).$$

Hence, we have

$$RS(\mathbf{x}, \mathbf{q}) = \sum_{n=1}^{N_b} \sum_{j=1}^{N_y} c_{nj}(\mathbf{x}) \frac{2\sqrt{\alpha_{nl(j)}}}{\sqrt{\pi\tau^3 J_{l(j)+3/2}(\alpha_{nl(j)})}} j_{l(j)} \left( \frac{\alpha_{nl(j)} |\mathbf{q}|}{\tau} \right) Y_j \left( R^{-1} \frac{\mathbf{q}}{|\mathbf{q}|} \right).$$

This indicates that the rotation reorientation of mDWI is equivalent to applying the rotation transformation to the real spherical harmonics,  $Y_j$ . According to the work in Geng et al. (2011) and

Edmonds (1996), the rotation of  $Y_j$  can be achieved by the rotation of their corresponding coefficients, yielding

$$RS(\mathbf{x}, \mathbf{q}) = \sum_{n=1}^{N_b} \left( \sum_{j=1}^{N_y} \left( \sum_{j'=1}^{N_y} M_{jj'} c_{nj'}(\mathbf{x}) \right) \right) \frac{2\sqrt{\alpha_{nl(j)}}}{\sqrt{\pi\tau^3 J_{l(j)+3/2}(\alpha_{nl(j)})}} j_{l(j)} \left( \frac{\alpha_{nl(j)} |\mathbf{q}|}{\tau} \right) Y_j \left( \frac{\mathbf{q}}{|\mathbf{q}|} \right), \quad (4)$$

where  $M_{jj'}$  is the  $jj'$ th element of Wigner matrix  $M(R)$  constructed based on  $R$  (see details in Geng et al. (2011) and Edmonds (1996)). We can see that the same Wigner matrix is applied to  $c_{nj}$  at a fixed  $n$ . For the sake of simplicity, we rewrite Eq. (4) in the matrix form, i.e.,

$$RS(\mathbf{x}, \mathbf{q}) = (\mathbf{M}(R) \mathbf{c}(\mathbf{x}))^\top \Psi(\mathbf{q}), \quad (5)$$

where  $\mathbf{M}$  is a sparse matrix with  $N_b$  diagonal blocks of  $M(R)$ .  $\mathbf{c}$  is a vector that concatenates coefficients  $c_{nj}$  in the order such that  $c_{nj}$  corresponds to  $M(R)$  at a fixed  $n$ .  $\Psi(\mathbf{q})$  concatenates the BFOR signal basis.

#### 3.2. Diffeomorphic group action on $S(\mathbf{x}, \mathbf{q})$

We define an action of diffeomorphisms  $\phi: \Omega \rightarrow \Omega$  on  $S(\mathbf{x}, \mathbf{q})$ , which takes into consideration of the reorientation in the  $q$ -space as well as the transformation of the spatial volume in  $\Omega$ . Based on the rotation reorientation of  $S(\mathbf{x}, \mathbf{q})$  in Eq. (5), for a given spatial location  $\mathbf{x}$ , the action of  $\phi$  on  $S(\mathbf{x}, \mathbf{q})$  can be defined as

$$\phi \cdot S(\mathbf{x}, \mathbf{q}) = S\left(\phi^{-1}(\mathbf{x}), R_{\phi^{-1}(\mathbf{x})}^{-1} \mathbf{q}\right) = \left(\mathbf{M}\left(R_{\phi^{-1}(\mathbf{x})}\right) \mathbf{c}\left(\phi^{-1}(\mathbf{x})\right)\right)^\top \Psi(\mathbf{q}),$$

where  $R_{\mathbf{x}}$  can be defined in a way similar to the finite strain scheme used in DTI registration (Alexander et al., 2001). That is,  $R_{\mathbf{x}} = (D_{\mathbf{x}}\phi D_{\mathbf{x}}^\top \phi)^{-1} D_{\mathbf{x}}\phi$ , where  $D_{\mathbf{x}}\phi$  is the Jacobian matrix of  $\phi$  at  $\mathbf{x}$ . For the remainder of this paper, we denote this as

$$\phi \cdot S(\mathbf{x}, \mathbf{q}) = (\mathbf{M}(R_{\mathbf{x}}) \mathbf{c})^\top \circ \phi^{-1}(\mathbf{x}) \Psi(\mathbf{q}), \quad (6)$$

where  $\circ$  indicates as the composition of diffeomorphisms.

#### 3.3. Large deformation diffeomorphic metric mapping for HYDIs

Based on the BFOR representation of  $S(\mathbf{x}, \mathbf{q})$  and the diffeomorphic group action on  $S(\mathbf{x}, \mathbf{q})$ , we now state a variational problem for mapping HYDIs from one subject to another. We define this problem in the "large deformation" setting of Grenander's group action approach for modeling the white matter anatomy, that is, the HYDI data are modeled by assuming that they can be generated from one to another via flows of diffeomorphisms,  $\phi_t$ , which are the solutions of ordinary differential equations,  $\dot{\phi}_t = v_t(\phi_t)$ ,  $t \in [0, 1]$ , starting from the identity map  $\phi_0 = \text{Id}$ . They are therefore characterized by time-dependent velocity vector fields  $v_t$ ,  $t \in [0, 1]$ . We define a metric distance between a HYDI volume of a subject,  $S^{(s)}$ , and an atlas HYDI volume,  $S^{\text{atlas}}$ , as the minimal length of curves  $\phi_t \cdot S^{\text{atlas}}$ ,  $t \in [0, 1]$ , in a shape space such that, at time  $t=1$ ,  $\phi_1 \cdot S^{\text{atlas}} = S^{(s)}$ . Lengths of such curves are computed as the integrated norm  $\|v_t\|_V$  of the vector field generating the transformation, where  $v_t \in V$  and  $V$  is a reproducing kernel Hilbert space with kernel  $k_V$  and norm  $\|\cdot\|_V$ . To ensure solutions are diffeomorphic,  $V$  must be a space of smooth vector fields. Using the duality isometry in Hilbert spaces, one can equivalently express the lengths in terms of  $m_t$ , interpreted as momentum, such that for each  $u \in V$ ,

$$\langle m_t, u \circ \phi_t \rangle_2 = \langle k_V^{-1} v_t, u \rangle_2,$$

where we let  $\langle m, u \rangle_2$  denote the  $L^2$  inner product between  $m$  and  $u$ , but also, with a slight abuse, the result of the natural pairing between  $m$  and  $v$  in cases where  $m$  is singular (e.g., a measure). This

identity is classically written as  $\phi_t^* m_t = k_V^{-1} v_t$ , where  $\phi_t^*$  is referred to as the pullback operation on a vector measure,  $m_t$ . Using the identity  $\|v_t\|_V^2 = \langle k_V^{-1} v_t, v_t \rangle_2 = \langle m_t, k_V m_t \rangle_2$  and the standard fact that energy-minimizing curves coincide with constant-speed length-minimizing curves, one can obtain the metric distance between the atlas and target volumes by minimizing  $\int_0^1 \langle m_t, k_V m_t \rangle_2 dt$  such that  $\phi_1 \cdot S^{\text{atlas}} \approx S^{(s)}$  at  $t = 1$ . We associate this with a variational problem in the form of

$$J(m_t) = \inf_{m_t: \phi_t = k_V m_t(\phi_t), \phi_0 = \text{Id}} \int_0^1 \langle m_t, k_V m_t \rangle_2 dt + \lambda E(\phi_1 \cdot S^{\text{atlas}}, S^{(s)}), \quad (7)$$

where  $\lambda$  is a positive scalar.  $E$  quantifies the difference between the deformed atlas  $\phi_1 \cdot S^{\text{atlas}}$  and the subject  $S^{(s)}$ . Based on Eqs. (3) and (6),  $E$  is expressed in the form of

$$E = \int_{\mathbf{x} \in \Omega} \|(\mathbf{M}(R_{\mathbf{x}}) \mathbf{c}^{\text{atlas}}) \circ \phi^{-1}(\mathbf{x}) - \mathbf{c}^{(s)}(\mathbf{x})\|_2^2 d\mathbf{x}. \quad (8)$$

### 3.4. Gradient of $J$ with respect to $m_t$

We now solve the optimization problem in Eq. (7) via a gradient descent method. The gradient of  $J$  with respect to  $m_t$  can be computed via studying a variation  $m_t^\epsilon = m_t + \epsilon \tilde{m}_t$  on  $J$  such that the derivative of  $J$  with respect to  $\epsilon$  is expressed in function of  $\tilde{m}_t$ . According to the general LDDMM framework derived in Du et al. (2011), we directly give the expression of the gradient of  $J$  with respect to  $m_t$  as

$$\nabla J(m_t) = 2m_t + \lambda \eta_t, \quad (9)$$

where

$$\eta_t = \nabla_{\phi_1} E + \int_t^1 [\partial_{\phi_s}(k_V m_s)]^\top (\eta_s + m_s) ds. \quad (10)$$

Eq. (10) can be solved backward given  $\eta_1 = \nabla_{\phi_1} E$ .  $\partial_{\phi_s}(k_V m_s)$  is the partial derivative of  $k_V m_s$  with respect to  $\phi_s$ .

In the following, we discuss the computation of  $\nabla_{\phi_1} E$ . We consider a variation of  $\phi_1$  as  $\phi_1^\epsilon = \phi_1 + \epsilon h$  and denote the corresponding variation in  $\mathbf{M}(R_{\mathbf{x}})$  as  $\mathbf{M}(R_{\mathbf{x}}^\epsilon)$ . Denote  $\hat{\mathbf{c}}(\mathbf{x}) = \mathbf{M}(R_{\mathbf{x}}) \mathbf{c}^{\text{atlas}}(\mathbf{x})$  for the simplicity of notation. We have

$$\begin{aligned} \left. \frac{\partial E}{\partial \epsilon} \right|_{\epsilon=0} &= \int_{\mathbf{x} \in \Omega} \left. \frac{\partial \|(\mathbf{M}(R_{\mathbf{x}}^\epsilon) \mathbf{c}^{\text{atlas}}) \circ (\phi_1^\epsilon)^{-1}(\mathbf{x}) - \mathbf{c}^{(s)}(\mathbf{x})\|_2^2}{\partial \epsilon} \right|_{\epsilon=0} d\mathbf{x} \\ &= 2 \int_{\mathbf{x} \in \Omega} \left\langle \underbrace{\hat{\mathbf{c}} \circ \phi_1^{-1}(\mathbf{x}) - \mathbf{c}^{(s)}(\mathbf{x})}_{\text{term(A)}}, \nabla_{\mathbf{x}}^\top \hat{\mathbf{c}} \circ \phi_1^{-1}(\mathbf{x}) \left. \frac{\partial (\phi_1^\epsilon)^{-1}}{\partial \epsilon} \right|_{\epsilon=0} \right\rangle d\mathbf{x} \\ &\quad + 2 \int_{\mathbf{x} \in \Omega} \left\langle \hat{\mathbf{c}} \circ \phi_1^{-1}(\mathbf{x}) - \mathbf{c}^{(s)}(\mathbf{x}), \underbrace{\left( \left. \frac{\partial \mathbf{M}(R_{\mathbf{x}}^\epsilon) \mathbf{c}^{\text{atlas}}}{\partial \epsilon} \right|_{\epsilon=0} \right) \circ \phi_1^{-1}(\mathbf{x})}_{\text{term(B)}} \right\rangle d\mathbf{x}. \end{aligned} \quad (11)$$

The calculation of Term (A) is straightforward. We have  $\left. \frac{\partial (\phi_1^\epsilon)^{-1}}{\partial \epsilon} \right|_{\epsilon=0} = -[(D_{\mathbf{x}} \phi_1)^{-1} h] \circ \phi_1^{-1}$  derived from the fact of  $\phi_1^\epsilon \circ (\phi_1^\epsilon)^{-1} = \text{Id}$ . Applying the strategy of the change of variable,  $\mathbf{y} = \phi_1^{-1}(\mathbf{x})$ , we have

$$\text{Term(A)} = -2 \int_{\mathbf{y} \in \Omega} \langle \hat{\mathbf{c}}(\mathbf{y}) - \mathbf{c}^{(s)} \circ \phi_1(\mathbf{y}), \nabla_{\mathbf{y}}^\top \hat{\mathbf{c}}(\mathbf{y}) [(D_{\mathbf{y}} \phi_1)^{-1} h] \det(D_{\mathbf{y}} \phi_1) \rangle d\mathbf{y}$$

Hence,

$$\text{Term(A)} = -2 \int_{\mathbf{x} \in \Omega} \langle (D_{\mathbf{x}} \phi_1)^{-\top} \nabla_{\mathbf{x}} \hat{\mathbf{c}}(\mathbf{x}) (\hat{\mathbf{c}}(\mathbf{x}) - \mathbf{c}^{(s)} \circ \phi_1(\mathbf{x})) \det(D_{\mathbf{x}} \phi_1), h \rangle d\mathbf{x}. \quad (12)$$

This is similar to that in the scalar image mapping case. It seeks the optimal spatial transformation  $\phi_t$  in the gradient direction of image  $\hat{\mathbf{c}}(\mathbf{x})$  weighted by the difference between the atlas and subject's images.

The computation of Term (B) involves the derivative of  $\mathbf{M}(R_{\mathbf{x}})$  with respect to a rotation matrix,  $R_{\mathbf{x}}$ , and the variation of  $R_{\mathbf{x}}^\epsilon$  with respect to the small variation of  $\phi_1^\epsilon$ . Let's first compute the derivative of  $\mathbf{M}(R_{\mathbf{x}})$  with respect to  $R_{\mathbf{x}}$ . According to the work in Cetingul et al. (2012), the analytical form of this derivative can be solved using the Euler angle representation of  $R_{\mathbf{x}}$  but is relatively complex. Here, we consider Wigner matrix  $\mathbf{M}(R_{\mathbf{x}})$  and the coefficients of the BFOR signal basis  $\mathbf{c}^{\text{atlas}}(\mathbf{x})$  together, which leads to a simple numeric approach for computing the derivative of  $\hat{\mathbf{c}}(\mathbf{x}) = \mathbf{M}(R_{\mathbf{x}}) \mathbf{c}^{\text{atlas}}(\mathbf{x})$  with respect to  $R_{\mathbf{x}}$ , i.e.,  $\nabla_{R_{\mathbf{x}}} \hat{\mathbf{c}}(\mathbf{x})$ . Assume  $\tilde{R}_{\mathbf{x}} = e^{\delta U} R_{\mathbf{x}}$  where  $\delta U = \begin{bmatrix} 0 & -\delta\mu_3 & \delta\mu_2 \\ \delta\mu_3 & 0 & -\delta\mu_1 \\ -\delta\mu_2 & \delta\mu_1 & 0 \end{bmatrix}$  is a skew-symmetric matrix parameterized by  $\delta\boldsymbol{\mu} = [\delta\mu_1 \ \delta\mu_2 \ \delta\mu_3]^\top$ . From this construction,  $\delta U$  is the tangent vector at  $R_{\mathbf{x}}$  on the manifold of rotation matrices and  $\tilde{R}_{\mathbf{x}}$  is also a rotation matrix. Based on the Taylor expansion, we have the first order approximation of  $\mathbf{M}(\tilde{R}_{\mathbf{x}}) \mathbf{c}^{\text{atlas}}(\mathbf{x})$  as

$$\mathbf{M}(\tilde{R}_{\mathbf{x}}) \mathbf{c}^{\text{atlas}}(\mathbf{x}) \approx \hat{\mathbf{c}}(\mathbf{x}) + \nabla_{R_{\mathbf{x}}}^\top \hat{\mathbf{c}}(\mathbf{x}) \delta\boldsymbol{\mu}.$$

We can compute  $\nabla_{R_{\mathbf{x}}} \hat{\mathbf{c}}(\mathbf{x})$  as follows. Assume  $\delta U_1, \delta U_2, \delta U_3$  to be skew-symmetric matrices respectively constructed from  $[\delta\mu_1, 0, 0]^\top, [0, \delta\mu_2, 0]^\top, [0, 0, \delta\mu_3]^\top$ . We have

$$\nabla_{R_{\mathbf{x}}} \hat{\mathbf{c}}(\mathbf{x}) \approx \begin{bmatrix} (\mathbf{M}(e^{\delta U_1} R_{\mathbf{x}}) \mathbf{c}^{\text{atlas}}(\mathbf{x}) - \hat{\mathbf{c}}(\mathbf{x}))^\top / \delta\mu_1 \\ (\mathbf{M}(e^{\delta U_2} R_{\mathbf{x}}) \mathbf{c}^{\text{atlas}}(\mathbf{x}) - \hat{\mathbf{c}}(\mathbf{x}))^\top / \delta\mu_2 \\ (\mathbf{M}(e^{\delta U_3} R_{\mathbf{x}}) \mathbf{c}^{\text{atlas}}(\mathbf{x}) - \hat{\mathbf{c}}(\mathbf{x}))^\top / \delta\mu_3 \end{bmatrix}. \quad (13)$$

We now compute the variation of  $R_{\mathbf{x}}^\epsilon$  with respect to the small variation of  $\phi_1^\epsilon$ . This has been referred as exact finite-strain differential that was solved in Dorst (2005) and applied to the DTI tensor-based registration in Yeo et al. (2009). Here, we directly adopt the result from Yeo et al. (2009) and obtain

$$\left. \frac{\partial R_{\mathbf{x}}^\epsilon}{\partial \epsilon} \right|_{\epsilon=0} = -F_{\mathbf{x}} \sum_{i=1}^3 [\mathbf{r}_i \times (D_{\mathbf{x}} h^\top)_i], \quad (14)$$

where  $F_{\mathbf{x}} = -R_{\mathbf{x}}^\top (\text{trace}((D_{\mathbf{x}} \phi_1 D_{\mathbf{x}}^\top \phi_1)^{1/2}) \text{Id} - (D_{\mathbf{x}} \phi_1 D_{\mathbf{x}}^\top \phi_1)^{1/2})^{-1} R_{\mathbf{x}}$ .  $\times$  denotes as the cross product of two vectors.  $(A)_i$  denotes the  $i$ th column of matrix  $A$ .  $\mathbf{r}_i = (R_{\mathbf{x}}^\top)_i$ .

Given Eqs. (13) and (14), we thus have

$$\begin{aligned} \text{Term(B)} &= -2 \int_{\mathbf{x} \in \Omega} \left\langle \hat{\mathbf{c}} \circ \phi_1^{-1}(\mathbf{x}) - \mathbf{c}^{(s)}(\mathbf{x}), \left( \nabla_{R_{\mathbf{x}}} \hat{\mathbf{c}}^\top F_{\mathbf{x}} \sum_{i=1}^3 [\mathbf{r}_i \times (D_{\mathbf{x}} h^\top)_i] \right) \circ \phi_1^{-1} \right\rangle d\mathbf{x} \\ &= -2 \int_{\mathbf{x} \in \Omega} \omega_{\mathbf{x}}^\top \sum_{i=1}^3 [\mathbf{r}_i \times (D_{\mathbf{x}} h^\top)_i] d\mathbf{x} = -2 \int_{\mathbf{x} \in \Omega} \sum_{i=1}^3 (\omega_{\mathbf{x}} \times \mathbf{r}_i, \nabla_{\mathbf{x}} h_i) d\mathbf{x}, \end{aligned} \quad (15)$$

where

$$\omega_{\mathbf{x}}^\top = (\nabla_{R_{\mathbf{x}}} \hat{\mathbf{c}}(\mathbf{x}) (\hat{\mathbf{c}}(\mathbf{x}) - \mathbf{c}^{(s)} \circ \phi_1(\mathbf{x})))^\top F_{\mathbf{x}} \det(D_{\mathbf{x}} \phi_1), \quad (16)$$

and  $h = [h_1 \ h_2 \ h_3]^\top$ .  $D_{\mathbf{x}} h$  is approximated as

$$D_{\mathbf{x}} h = \begin{bmatrix} \nabla_{\mathbf{x}} h_1^\top \\ \nabla_{\mathbf{x}} h_2^\top \\ \nabla_{\mathbf{x}} h_3^\top \end{bmatrix} \approx \frac{1}{2\Delta d} \begin{bmatrix} h_{1,\mathbf{x}^{\text{x}^+}} - h_{1,\mathbf{x}^{\text{x}^-}} & h_{1,\mathbf{x}^{\text{y}^+}} - h_{1,\mathbf{x}^{\text{y}^-}} & h_{1,\mathbf{x}^{\text{z}^+}} - h_{1,\mathbf{x}^{\text{z}^-}} \\ h_{2,\mathbf{x}^{\text{x}^+}} - h_{2,\mathbf{x}^{\text{x}^-}} & h_{2,\mathbf{x}^{\text{y}^+}} - h_{2,\mathbf{x}^{\text{y}^-}} & h_{2,\mathbf{x}^{\text{z}^+}} - h_{2,\mathbf{x}^{\text{z}^-}} \\ h_{3,\mathbf{x}^{\text{x}^+}} - h_{3,\mathbf{x}^{\text{x}^-}} & h_{3,\mathbf{x}^{\text{y}^+}} - h_{3,\mathbf{x}^{\text{y}^-}} & h_{3,\mathbf{x}^{\text{z}^+}} - h_{3,\mathbf{x}^{\text{z}^-}} \end{bmatrix},$$

where  $\{\mathbf{x}^{\text{x}^+}, \mathbf{x}^{\text{x}^-}, \mathbf{x}^{\text{y}^+}, \mathbf{x}^{\text{y}^-}, \mathbf{x}^{\text{z}^+}, \mathbf{x}^{\text{z}^-}\}$  are the neighbors of  $\mathbf{x}$  in  $x, y, z$  directions, respectively.  $\Delta d$  is the distance of these neighbors to  $\mathbf{x}$ . Here, term (B) seeks the spatial transformation  $\phi_t$  such that the

local diffusion profiles of the atlas and subject's HYDIs have to be aligned.

In summary, we have

$$\begin{aligned} \frac{\partial E}{\partial \epsilon} \Big|_{\epsilon=0} &\approx -2 \int_{\mathbf{x} \in \Omega} \langle (D_{\mathbf{x}} \phi_1)^{-T} \nabla_{\mathbf{x}} \hat{\mathbf{c}}(\mathbf{x}) (\hat{\mathbf{c}}(\mathbf{x}) - \mathbf{c}^{(s)} \circ \phi_1(\mathbf{x})) \det(D_{\mathbf{x}} \phi_1), h \rangle d\mathbf{x} \\ &- \frac{1}{\Delta d} \int_{\mathbf{x} \in \Omega} \sum_{k=1}^3 \left\langle \left\langle \omega_{\mathbf{x}} \times \mathbf{r}_k, \begin{bmatrix} h_{k,x^+} \\ h_{k,x^y} \\ h_{k,x^z} \end{bmatrix} \right\rangle - \left\langle \omega_{\mathbf{x}} \times \mathbf{r}_k, \begin{bmatrix} h_{k,x^-} \\ h_{k,x^y} \\ h_{k,x^z} \end{bmatrix} \right\rangle \right\rangle d\mathbf{x}. \end{aligned} \quad (17)$$

Therefore,  $\nabla_{\phi_1} E$  can be obtained from Eq. (17).

### 3.5. Numerical implementation

We so far derive  $J$  and its gradient  $\nabla J(m_t)$  in the continuous setting. In this section, we elaborate the numerical implementation of our algorithm under the discrete setting. Since HYDI DW signals were represented using the orthonormal BFOR signal bases, both the computation of  $J$  in Eq. (7) and the gradient computation in Eq. (17) do not explicitly involve the calculation  $\Psi(\mathbf{q})$ . Hence, we do not need to discretize the  $q$ -space. In the discretization of the image domain, we first represent the ambient space,  $\Omega$ , using a finite number of points on the image grid,  $\Omega \cong \{(\mathbf{x}_i)_{i=1}^N\}$ . In this setting, we can assume  $m_t$  to be the sum of Dirac measures, where  $\alpha_i(t)$  is the momentum vector at  $\mathbf{x}_i$  and time  $t$ . We use a conjugate gradient routine to perform the minimization of  $J$  with respect to  $\alpha_i(t)$ . We summarize steps required in each iteration during the minimization process below:

1. Use the forward Euler method to compute the diffeomorphic trajectory based on the flow equation:

$$\frac{d\phi_t(\mathbf{x}_i)}{dt} = \sum_{j=1}^N k_V(\phi_t(\mathbf{x}_i), \phi_t(\mathbf{x}_j)) \alpha_j(t). \quad (18)$$

That is,

$$\phi_{t+1}(\mathbf{x}_i) = \phi_t(\mathbf{x}_i) + dt \sum_{j=1}^N k_V(\phi_t(\mathbf{x}_i), \phi_t(\mathbf{x}_j)) \alpha_j(t),$$

where  $dt$  is the step size.

2. Compute  $\nabla_{\phi_1(\mathbf{x}_i)} E$  based on Eq. (17).
3. Solve  $\eta_t = [\eta_i(t)]_{i=1}^N$  in Eq. (10) using the backward Euler integration, where  $i$  indices  $\mathbf{x}_i$ , with the initial condition  $\eta_i(1) = \nabla_{\phi_1(\mathbf{x}_i)} E$ . Hence, numerically,

$$\eta_t = \eta_{t+1} + [\partial_{\phi_{t+1}}(k_V m_{t+1})]^T (\eta_{t+1} + m_{t+1}) dt,$$

where  $dt$  is the step size.

4. Compute gradient  $\nabla J(\alpha_i(t)) = 2\alpha_i(t) + \eta_i(t)$ .
5. Evaluate  $J$  when  $\alpha_i(t) = \alpha_i^{\text{old}}(t) - \epsilon \nabla J(\alpha_i(t))$ , where  $\epsilon$  is the adaptive step size determined by a golden section search.

## 4. Bayesian HYDI atlas estimation

In the above LDDMM-HYDI algorithm, we assume that the atlas,  $S^{\text{atlas}}$ , is known. In this section, we introduce a HYDI atlas estimation approach based on Bayesian decision theory. Given  $n$  observed HYDI datasets,  $S^{(i)}$  for  $i = 1, \dots, n$ , we assume that each of them can be estimated through an unknown atlas  $S^{\text{atlas}}$  and a diffeomorphic transformation  $\phi^{(i)}$  such that

$$S^{(i)} \approx \hat{S}^{(i)} = \phi^{(i)} \cdot S^{\text{atlas}}. \quad (19)$$

The variation of  $S^{(i)}$  relative to  $\hat{S}^{(i)}$  is then denoted by  $\sigma^2$ . The goal here is to estimate the unknown atlas,  $S^{\text{atlas}}$ , and the variation,  $\sigma^2$ . To solve this problem, we first introduce an ancillary ‘‘hyperatlas’’

$S_0$ , and assume that our atlas is generated from it via a diffeomorphic transformation of  $\phi$  such that  $S^{\text{atlas}} = \phi \cdot S_0$ . The use of the hyperatlas guarantees the estimated atlas in the orbit of the hyperatlas. We use the Bayesian strategy to estimate  $\phi$  and  $\sigma^2$  from the set of observations  $S^{(i)}$ ,  $i = 1, \dots, n$  by computing the maximum a posteriori (MAP) of  $f_{\sigma}(\phi | S^{(1)}, S^{(2)}, \dots, S^{(n)}, S_0)$ . This can be achieved using the Expectation–Maximization algorithm by first computing the log-likelihood of the complete data  $(\phi, \phi^{(i)}, S^{(i)}, i = 1, 2, \dots, n)$  when  $\phi^{(1)}, \dots, \phi^{(n)}$  are introduced as hidden variables. We denote this likelihood as  $f_{\sigma}(\phi, \phi^{(1)}, \dots, \phi^{(n)}, S^{(1)}, \dots, S^{(n)} | S_0)$ . We consider that the paired information of individual observations,  $(S^{(i)}, \phi^{(i)})$  for  $i = 1, \dots, n$ , as independent and identically distributed. As a result, this log-likelihood can be written as

$$\begin{aligned} \log f_{\sigma}(\phi, \phi^{(1)}, \dots, \phi^{(n)}, S^{(1)}, \dots, S^{(n)} | S_0) &= \log f(\phi | S_0) \\ &+ \sum_{i=1}^n \{ \log f(\phi^{(i)} | \phi, S_0) + \log f_{\sigma}(S^{(i)} | \phi^{(i)}, \phi, S_0) \}, \end{aligned} \quad (20)$$

where  $f(\phi | S_0)$  is the shape prior (probability distribution) of the atlas given the hyperatlas,  $S_0$ .  $f(\phi^{(i)} | \phi, S_0)$  is the distribution of random diffeomorphisms given the estimated atlas  $(\phi \cdot S_0)$ .  $f_{\sigma}(S^{(i)} | \phi^{(i)}, \phi, S_0)$  is the conditional likelihood of the HYDI data given its corresponding hidden variable  $\phi^{(i)}$  and the estimated atlas  $(\phi \cdot S_0)$ . In the remainder of this section, we first adopt  $f(\phi | S_0)$  and  $f(\phi^{(i)} | \phi, S_0)$  introduced in Ma et al. (2008) and Qiu et al. (2010) under the framework of LDDMM and then describe how to calculate  $f_{\sigma}(S^{(i)} | \phi^{(i)}, \phi, S_0)$  in Section 4.2 based on the BFOR representation of HYDI.

### 4.1. The shape prior of the atlas and the distribution of random diffeomorphisms

We adopt the previous work in Ma et al. (2008) and Qiu et al. (2010) and briefly describe the construction of the shape prior (probability distribution) of the atlas,  $f(\phi | S_0)$ . Under the LDDMM framework, we can compute the prior  $f(\phi | S_0)$  via  $m_0$ , i.e.,

$$f(\phi | S_0) = f(m_0 | S_0), \quad (21)$$

where  $m_0$  is initial momentum defined in the coordinates of  $S_0$  such that it uniquely determines diffeomorphic geodesic flows from  $S_0$  to the estimated atlas. When  $S_0$  remains fixed, the space of the initial momentum  $m_0$  provides a linear representation of the nonlinear diffeomorphic shape space in which linear statistical analysis can be applied. Hence, assuming  $m_0$  is random, we immediately obtain a stochastic model for diffeomorphic transformations of  $S_0$ . More precisely, we follow the work in Ma et al. (2008) and Qiu et al. (2010) and assume  $m_0$  to be a centered Gaussian random field (GRF) model. The distribution of  $m_0$  is characterized by its covariance bilinear form, defined by

$$\Gamma_{m_0}(v, w) = E[m_0(v) m_0(w)],$$

where  $v, w$  are vector fields in the Hilbert space of  $V$  with reproducing kernel  $k_V$ .

We associate  $\Gamma_{m_0}$  with  $k_V^{-1}$ . The ‘‘prior’’ of  $m_0$  in this case is then

$$\frac{1}{\mathcal{Z}} \exp \left( -\frac{1}{2} \langle m_0, k_V m_0 \rangle_2 \right),$$

where  $\mathcal{Z}$  is the normalizing Gaussian constant. This leads to formally define the ‘‘log-prior’’ of  $m_0$  to be

$$\log f(m_0 | S_0) \approx -\frac{1}{2} \langle m_0, k_V m_0 \rangle_2, \quad (22)$$

where we ignore the normalizing constant term  $\log \mathcal{Z}$ .

We can construct the distribution of random diffeomorphisms,  $f(\phi^{(i)} | \phi, S_0)$ , in the similar manner. We define  $f(\phi^{(i)} | \phi, S_0)$  via the corresponding initial momentum  $m_0^{(i)}$  defined in the coordinates

of  $\phi \cdot S_0$ . We also assume that  $m_0^{(i)}$  is random, and therefore, we again obtain a stochastic model for *diffeomorphic transformations* of  $S^{\text{atlas}} \cong \phi \cdot S_0$ .  $m_0^{(i)}$  is assumed to be a centered GRF model with its covariance as  $k_V^\pi$ , where  $k_V^\pi$  is the reproducing kernel of the smooth vector field in a Hilbert space  $V$ . Hence, we can define the log distribution of random diffeomorphisms as

$$\log f(\phi^{(i)}|\phi, S_0) \approx -\frac{1}{2} \langle m_0^{(i)}; k_V^\pi m_0^{(i)} \rangle_2. \quad (23)$$

where as before, we ignore the normalizing constant term  $\log \mathcal{Z}$ .

#### 4.2. The conditional likelihood of the HYDI data

Given the representation of the diffusion signals in the  $q$ -space using the BFOR signal bases, we construct the conditional likelihood of the HYDI data,  $f_\sigma(S^{(i)}|\phi^{(i)}, \phi, S_0)$ , via the BFOR coefficients. We assume that  $\mathbf{c}_{ij}(\mathbf{x})$  has a multivariate Gaussian distribution with mean of  $\mathbf{c}^{\text{atlas}}(\mathbf{x})$  and covariance  $\sigma^2 \mathbf{I}_d$ , where  $\mathbf{c}^{\text{atlas}}(\mathbf{x})$  are the BFOR coefficients associated with  $S_{\text{atlas}}$  and  $\mathbf{I}_d$  is the identity matrix.

From the Gaussian assumption, we can thus write the conditional “log-likelihood” of  $S^{(i)}$  given  $S^{\text{atlas}}$  and  $\phi_1^{(i)}$  as

$$\log f_\sigma(S^{(i)}|\phi_1^{(i)}, \phi_1, S_0) \approx \int_{\mathbf{x} \in \Omega} \left\{ -\frac{1}{2\sigma^2} \left\| (\mathbf{M}(R_{\mathbf{x}}) \mathbf{c}^{\text{atlas}}) \circ (\phi_1^{(i)})^{-1}(\mathbf{x}) - \mathbf{c}^{(i)}(\mathbf{x}) \right\|^2 - \frac{\log \sigma^2}{2} \right\} d\mathbf{x}, \quad (24)$$

where as before, we ignore the normalizing Gaussian term.

#### 4.3. Expectation–maximization algorithm

In this section, we employ the Expectation–Maximization algorithm to estimate  $\sigma^2$  and the atlas,  $S^{\text{atlas}}(\mathbf{x}, \mathbf{q})$ , for  $\mathbf{q} \in \mathbb{R}^3, \mathbf{x} \in \Omega$ . From the above discussion, we first rewrite the log-likelihood function of the complete data in Eq. (20) as

$$\begin{aligned} \log f_\sigma(m_0, m_0^{(1)}, \dots, m_0^{(n)}, S^{(1)}, \dots, S^{(n)}|S_0) \\ \approx -\frac{1}{2} \langle m_0, k_V m_0 \rangle_2 - \sum_{i=1}^n \left\{ \frac{1}{2} \langle m_0^{(i)}, k_V^\pi m_0^{(i)} \rangle_2 \right. \\ \left. + \int_{\mathbf{x} \in \Omega} \left\{ \frac{1}{2\sigma^2} \left\| (\mathbf{M}(R_{\mathbf{x}}) \mathbf{c}^{\text{atlas}}) \circ (\phi_1^{(i)})^{-1}(\mathbf{x}) - \mathbf{c}^{(i)}(\mathbf{x}) \right\|^2 + \frac{\log \sigma^2}{2} \right\} d\mathbf{x} \right\}, \end{aligned} \quad (25)$$

where  $\mathbf{c}^{\text{atlas}}(\mathbf{x}) = (\mathbf{M}(R_{\mathbf{x}}) \mathbf{c}_0) \circ \phi_1^{-1}(\mathbf{x})$  computed based on Eq. (6).  $\mathbf{c}_0$  is the BFOR coefficients of the hyperatlas and  $\phi_1$  is the diffeomorphic transformation from the hyperatlas to the estimated atlas.

**The E-Step.** The E-step computes the expectation of the complete data log-likelihood given the previous atlas  $m_0^{\text{old}}$  and variance  $\sigma^{2\text{old}}$ . We denote this expectation as  $Q(m_0, \sigma^2|m_0^{\text{old}}, \sigma^{2\text{old}})$  given in the equation below,

$$\begin{aligned} Q(m_0, \sigma^2|m_0^{\text{old}}, \sigma^{2\text{old}}) &= E \left\{ \log f_\sigma(m_0, m_0^{(1)}, \dots, m_0^{(n)}, S^{(1)}, \dots, S^{(n)}|S_0) | m_0^{\text{old}}, \sigma^{2\text{old}}, S^{(1)}, \dots, S^{(n)}, S_0 \right\} \\ &\approx -\frac{1}{2} \langle m_0, k_V m_0 \rangle_2 - \sum_{i=1}^n E \left[ \frac{1}{2} \langle m_0^{(i)}, k_V^\pi m_0^{(i)} \rangle_2 + \int_{\mathbf{x} \in \Omega} \left\{ \frac{1}{2\sigma^2} \left\| (\mathbf{M}(R_{\mathbf{x}}) \mathbf{c}^{\text{atlas}}) \circ (\phi_1^{(i)})^{-1}(\mathbf{x}) - \mathbf{c}^{(i)}(\mathbf{x}) \right\|^2 \right. \right. \\ &\quad \left. \left. + \frac{\log \sigma^2}{2} \right\} d\mathbf{x} \right]. \end{aligned} \quad (26)$$

**The M-Step.** The M-step generates the new atlas by maximizing the  $Q$ -function with respect to  $m_0$  and  $\sigma^2$ . The update equation is given as

$$\begin{aligned} m_0^{\text{new}}, \sigma^{2\text{new}} &= \arg \max_{m_0, \sigma^2} Q(m_0, \sigma^2|m_0^{\text{old}}, \sigma^{2\text{old}}) \\ &= \arg \min_{m_0, \sigma^2} \left\{ \langle m_0, k_V m_0 \rangle_2 \right. \\ &\quad \left. + \sum_{i=1}^n E \left[ \int_{\mathbf{x} \in \Omega} \left\{ \frac{1}{\sigma^2} \left\| (\mathbf{M}(R_{\mathbf{x}}) \mathbf{c}^{\text{atlas}}) \circ (\phi_1^{(i)})^{-1}(\mathbf{x}) - \mathbf{c}^{(i)}(\mathbf{x}) \right\|^2 + \log \sigma^2 \right\} d\mathbf{x} \right] \right\}, \end{aligned} \quad (27)$$

where we use the fact that the conditional expectation of  $\langle m_0^{(i)}, k_V^\pi m_0^{(i)} \rangle_2$  is constant. We solve  $\sigma^2$  and  $m_0$  by separating the procedure for updating  $\sigma^2$  using the current value of  $m_0$ , and then optimizing  $m_0$  using the updated value of  $\sigma^2$ .

We now derive how to update values of  $\sigma^2$  and  $m_0$  from the  $Q$ -function in Eq. (27). It is straightforward to obtain  $\sigma^2$  by taking the derivative of  $Q(m_0, \sigma^2|m_0^{\text{old}}, \sigma^{2\text{old}})$  with respect to  $\sigma^2$  and setting it to zero (see Appendix A). Hence, we have

$$\sigma^{2\text{new}} = \frac{1}{n} \frac{1}{n_V} \sum_{i=1}^n \int_{\mathbf{x} \in \Omega} \left\| (\mathbf{M}(R_{\mathbf{x}}) \mathbf{c}^{\text{atlas}}) \circ (\phi_1^{(i)})^{-1}(\mathbf{x}) - \mathbf{c}^{(i)}(\mathbf{x}) \right\|^2 d\mathbf{x}, \quad (28)$$

where  $n_V$  is the number of voxels in  $\Omega$ .

For updating  $m_0$ , let  $\mathbf{y} = (\phi_1^{(i)})^{-1}(\mathbf{x})$  and  $|D\phi_1^{(i)}|$  be the Jacobian determinant of  $\phi_1^{(i)}$ . Using the change of variables strategy, we have

$$\begin{aligned} \sum_{i=1}^n E \left[ \int_{\mathbf{x} \in \Omega} \frac{1}{2\sigma^2} \left\| (\mathbf{M}(R_{\mathbf{x}}) \mathbf{c}^{\text{atlas}}) \circ (\phi_1^{(i)})^{-1}(\mathbf{x}) - \mathbf{c}^{(i)}(\mathbf{x}) \right\|^2 d\mathbf{x} \right] \\ = \sum_{i=1}^n E \left[ \int_{\mathbf{y} \in \Omega} \frac{1}{2\sigma^2} \left\| \mathbf{c}^{\text{atlas}}(\mathbf{y}) - (\mathbf{M}(R_{\mathbf{y}}) \mathbf{c}^{(i)}) \circ \phi_1^{(i)}(\mathbf{y}) \right\|^2 |D\phi_1^{(i)}(\mathbf{y})| d\mathbf{y} \right] \end{aligned} \quad (29)$$

We now introduce  $\bar{\mathbf{c}}_0(\mathbf{y})$  and assume

$$\bar{\mathbf{c}}_0(\mathbf{y}) = \frac{1}{\sum_{j=1}^n |D\phi_1^{(j)}(\mathbf{y})|} \sum_{i=1}^n |D\phi_1^{(i)}(\mathbf{y})| (\mathbf{M}(R_{\mathbf{y}}) \mathbf{c}^{(i)}) \circ \phi_1^{(i)}(\mathbf{y}), \quad (30)$$

Hence, Eq. (29) can be computed as

$$\begin{aligned} \int_{\mathbf{y} \in \Omega} \frac{1}{2\sigma^2} \sum_{i=1}^n E \left[ \left\| \mathbf{c}^{\text{atlas}}(\mathbf{y}) - \bar{\mathbf{c}}_0(\mathbf{y}) + \bar{\mathbf{c}}_0(\mathbf{y}) - (\mathbf{M}(R_{\mathbf{y}}) \mathbf{c}^{(i)}) \circ \phi_1^{(i)}(\mathbf{y}) \right\|^2 \right] d\mathbf{y} \\ = \int_{\mathbf{y} \in \Omega} \frac{1}{2\sigma^2} \sum_{i=1}^n E \left[ \left\{ \left\| \mathbf{c}^{\text{atlas}}(\mathbf{y}) - \bar{\mathbf{c}}_0(\mathbf{y}) \right\|^2 + \left\| \bar{\mathbf{c}}_0(\mathbf{y}) - (\mathbf{M}(R_{\mathbf{y}}) \mathbf{c}^{(i)}) \circ \phi_1^{(i)}(\mathbf{y}) \right\|^2 \right. \right. \\ \left. \left. + 2 \left\langle \mathbf{c}^{\text{atlas}}(\mathbf{y}) - \bar{\mathbf{c}}_0(\mathbf{y}), \bar{\mathbf{c}}_0(\mathbf{y}) - (\mathbf{M}(R_{\mathbf{y}}) \mathbf{c}^{(i)}) \circ \phi_1^{(i)}(\mathbf{y}) \right\rangle \right\} |D\phi_1^{(i)}(\mathbf{y})| \right] d\mathbf{y}. \end{aligned}$$

Since  $\bar{\mathbf{c}}_0(\mathbf{y})$  and  $(\mathbf{M}(R_{\mathbf{y}}) \mathbf{c}^{(i)}) \circ \phi_1^{(i)}(\mathbf{y})$  are only dependent on  $\phi_1^{(i)}$  and  $\sum_{i=1}^n |D\phi_1^{(i)}(\mathbf{y})| (\bar{\mathbf{c}}_0(\mathbf{y}) - (\mathbf{M}(R_{\mathbf{y}}) \mathbf{c}^{(i)}) \circ \phi_1^{(i)}(\mathbf{y})) = 0$ , we have

$$\begin{aligned} m_0^{\text{new}} &= \arg \min_{m_0} \frac{1}{2} \langle m_0, k_V m_0 \rangle_2 \\ &\quad + \frac{1}{2\sigma^{2\text{new}}} \int_{\mathbf{y} \in \Omega} \left[ \alpha(\mathbf{y}) \left\| \mathbf{c}^{\text{atlas}}(\mathbf{y}) - \bar{\mathbf{c}}_0(\mathbf{y}) \right\|^2 + \sum_{i=1}^n \left\| \bar{\mathbf{c}}_0(\mathbf{y}) \right. \right. \\ &\quad \left. \left. - (\mathbf{M}(R_{\mathbf{y}}) \mathbf{c}^{(i)}) \circ \phi_1^{(i)}(\mathbf{y}) \right\|^2 |D\phi_1^{(i)}(\mathbf{y})| \right] d\mathbf{y}, \end{aligned} \quad (31)$$

where  $\alpha(\mathbf{y}) = \sum_{i=1}^n |D\phi_1^{(i)}(\mathbf{y})|$ . Since the last term in Eq. (31) is not related to  $m_0$ , we have

$$\begin{aligned} m_0^{\text{new}} &= \arg \min_{m_0} \frac{1}{2} \langle m_0, k_V m_0 \rangle_2 + \frac{1}{2\sigma^{2\text{new}}} \int_{\mathbf{y} \in \Omega} \alpha(\mathbf{y}) \left\| \mathbf{c}^{\text{atlas}}(\mathbf{y}) \right. \\ &\quad \left. - \bar{\mathbf{c}}_0(\mathbf{y}) \right\|^2 d\mathbf{y}. \end{aligned}$$

Here  $\mathbf{c}^{\text{atlas}}(\mathbf{y}) = (\mathbf{M}(R_{\mathbf{y}}) \mathbf{c}_0) \circ \phi_1^{-1}(\mathbf{y})$ , where  $\mathbf{c}_0$  corresponds to the BFOR coefficients of the hyperatlas. We finally have

$$\begin{aligned} m_0^{\text{new}} &= \arg \min_{m_0} \frac{1}{2} \langle m_0, k_V m_0 \rangle_2 + \frac{1}{2\sigma^{2\text{new}}} \int_{\mathbf{y} \in \Omega} \alpha(\mathbf{y}) \left\| (\mathbf{M}(R_{\mathbf{y}}) \mathbf{c}_0) \right. \\ &\quad \left. \circ \phi_1^{-1}(\mathbf{y}) - \bar{\mathbf{c}}_0(\mathbf{y}) \right\|^2 d\mathbf{y}. \end{aligned} \quad (32)$$

The variational problem listed in Eq. (32) is referred as “modified LDDMM-HYDI mapping”, where weight  $\alpha$  is introduced. It can be easily solved by adopting the LDDMM-HYDI algorithm in Section 3. We present the steps involved in the EM optimization in Algorithm 1.

**Table 1**  
HYDI encoding scheme for human datasets.

Shell	Ne	$q$ ( $\text{mm}^{-1}$ )	$\Delta q$ ( $\text{mm}^{-1}$ )	$b$ ( $\text{s}/\text{mm}^2$ )
	7	0		0
1st	6	15.79	15.79	300
2nd	21	31.58	15.79	1200
3rd	24	47.37	15.79	2700
4th	24	63.16	15.79	4800
5th	50	78.95	15.79	7500
Total = 132		$q_{\max}=78.95$	Mean = 15.79	$b_{\max}=7500$

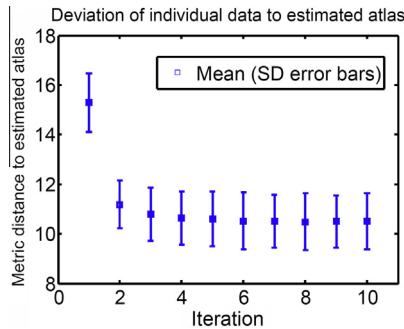


**Fig. 1.** The mean and standard deviation (SD) of the diffeomorphic metric between individual subjects and the estimated atlas at each iteration of the atlas generation optimization.

**Algorithm 1.** (The EM Algorithm for the HYDI Atlas Generation)

We initialize  $m_0 = 0$ . Thus, the hyperatlas  $S_0$  is considered as the initial atlas. In our case, we randomly select a subject's HYDI dataset as  $S_0$ .

1. Apply the LDDMM-HYDI mapping algorithm in Section 3 to register the current atlas to individual HYDI datasets, which yield  $m_0^{(i)}$  and  $\phi_t^{(i)}$ .
2. Compute  $\bar{c}_0$  according to Eq. (30).
3. Update  $\sigma^2$  according to Eq. (28).
4. Estimate  $S^{\text{atlas}} = \phi_1 \cdot S_0$ , where  $\phi_t$  is found by applying the modified LDDMM-HYDI mapping algorithm as given in Eq. (32).

The above computation is repeated until the atlas converges.

**5. Experiments**

In this section, we show the atlas generated using Algorithm 1, evaluate the LDDMM-HYDI mapping accuracy, and compare it with that of the diffeomorphic mapping for multiple diffusion tensors where the tensors are generated from each shell of the  $q$ -space. This diffeomorphic mapping algorithm for multiple diffusion tensors were adopted from the one in Cao et al. (2005). The experiments were performed on 36 human brain datasets (age:  $61.8 \pm 6.47$  years) acquired using a 3.0T GE-SIGNA scanner with an 8-channel head coil and ASSET parallel imaging (TE = 122 ms, TR = 12 s, FOV =  $256 \times 256$ , matrix =  $128 \times 128$ ). The datasets were

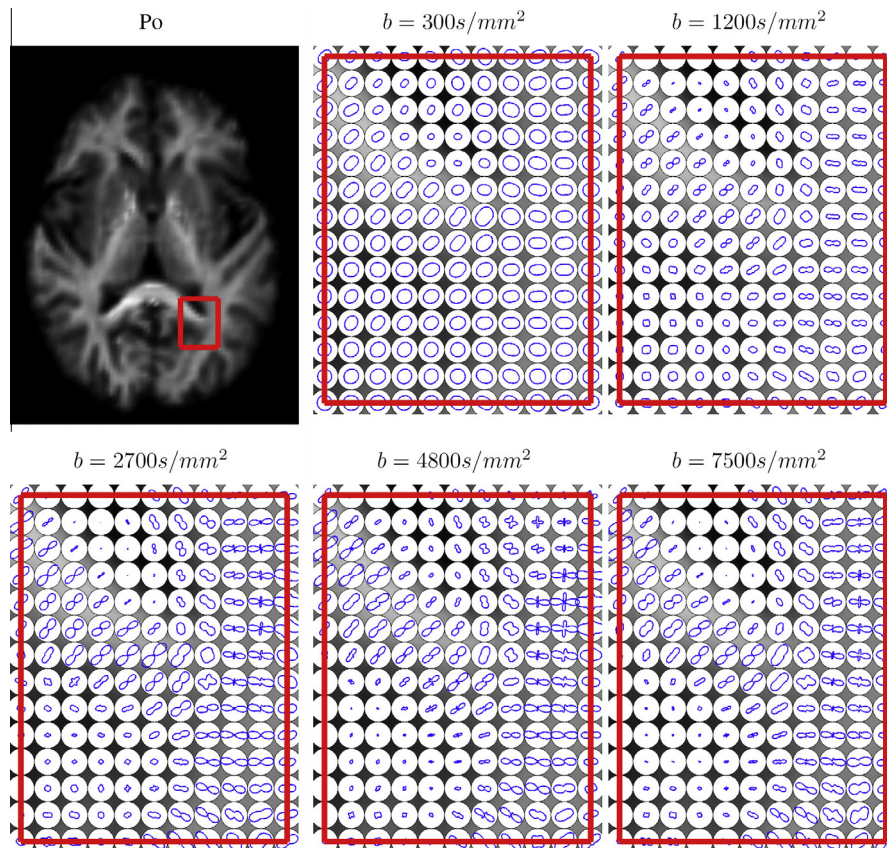


**Fig. 2.** Illustration of the estimated HYDI atlas in the  $q$ -space. The first panel shows the atlas of the zero displacement probability ( $P_0$ ) image in the axial view as the brain anatomical illustration. The rest panels show the diffusion profiles in the region of interest (red frame) at individual shells with  $b = 300, 1200, 2700, 4800,$  and  $7500 \text{ s}/\text{mm}^2$  in the  $q$ -space. Note that the profile of the diffusion weighted signals is orthogonal to the fiber orientation. (For interpretation of the references to color in this figure legend, the reader is referred to the web version of this article.)

acquired using a hybrid, non-Cartesian sampling scheme (Wu and Alexander, 2007). The HYDI encoding scheme is described in Table 1. Since the EAP reconstruction is sensitive to the angular resolution, the number of directions in the outer shells was increased to better characterize complex tissue organization (see Table 1). In the experiments of the atlas generation and LDDMM-HYDI evaluation, we represented HYDI DW signals using the BFOR signal basis with up to the fourth order modified SH bases and up to the sixth order spherical Bessel functions. The corresponding BFOR expansion coefficients were used in the atlas generation and LDDMM-HYDI optimization.

### 5.1. HYDI atlas

In the experiment of the atlas generation, we first chose one HYDI dataset as hyperatlas and assumed  $m_0 = 0$  such that the hyperatlas was used as the initial atlas. We then followed Algorithm 1 and repeated it for ten iterations. Notice that  $k_V$  associated with the covariance of  $m_0$  and  $k_V^\pi$  associated with the covariance of  $m_0^{(i)}$  were known and predetermined. Since we were dealing with vector fields in  $\mathbb{R}^3$ , the kernel of  $V$  is a matrix kernel operator in order to get a proper definition. Making an abuse of notation, we defined  $k_V$  and  $k_V^\pi$  respectively as  $k_V \mathbb{I}_{3 \times 3}$  and  $k_V^\pi \mathbb{I}_{3 \times 3}$ , where  $\mathbb{I}_{3 \times 3}$  is a  $3 \times 3$  identity matrix and  $k_V$  and  $k_V^\pi$  are scalars. In particular, we

assumed that  $k_V$  and  $k_V^\pi$  are Gaussian with kernel sizes of  $\sigma_V$  and  $\sigma_{V^\pi}$ . Since  $\sigma_V$  determines the smoothness level of the mapping from the hyperatlas to the averaged atlas in Eq. (32), whereas  $\sigma_{V^\pi}$  determines that from the atlas to individual HYDI datasets in Eq. (7). Hence,  $\sigma_V$  should be greater than  $\sigma_{V^\pi}$ . Upto now, there is no procedure to automatically optimize  $\sigma_V$  and  $\sigma_{V^\pi}$ . We thus empirically determined  $\sigma_{V^\pi} = 10$  and  $\sigma_V = 12$ .

First, we experimentally demonstrate the convergence of the diffeomorphic metric between individual subjects and the estimated atlas. This is measured using the square root of the inner product of the initial momentum. Fig. 1 shows the mean diffeomorphic metric of individual subjects referenced to the estimated atlas as well as its standard deviation across the subjects. From Fig. 1, we observe that the average diffeomorphic metric changed less than 5% after two iterations.

Next, we illustrate the atlas estimated from the 36 adults' HYDI datasets after ten iterations. Fig. 2 illustrates the estimated atlas of the diffusion signals at shells of  $b = 300, 1200, 2700, 4800, 7500$  s/mm<sup>2</sup>. Fig. 3 shows the reconstructed EAP based on the coefficients of the estimated HYDI atlas. Each row respectively shows the estimated atlas in the axial, coronal, and sagittal views, while each column shows the zero displacement probability (Po) image derived from EAP and the diffusion profiles of this atlas at three layers of the EAP space,  $p = 5, 10, 15$   $\mu\text{m}$ . Fig. 4 demonstrates the

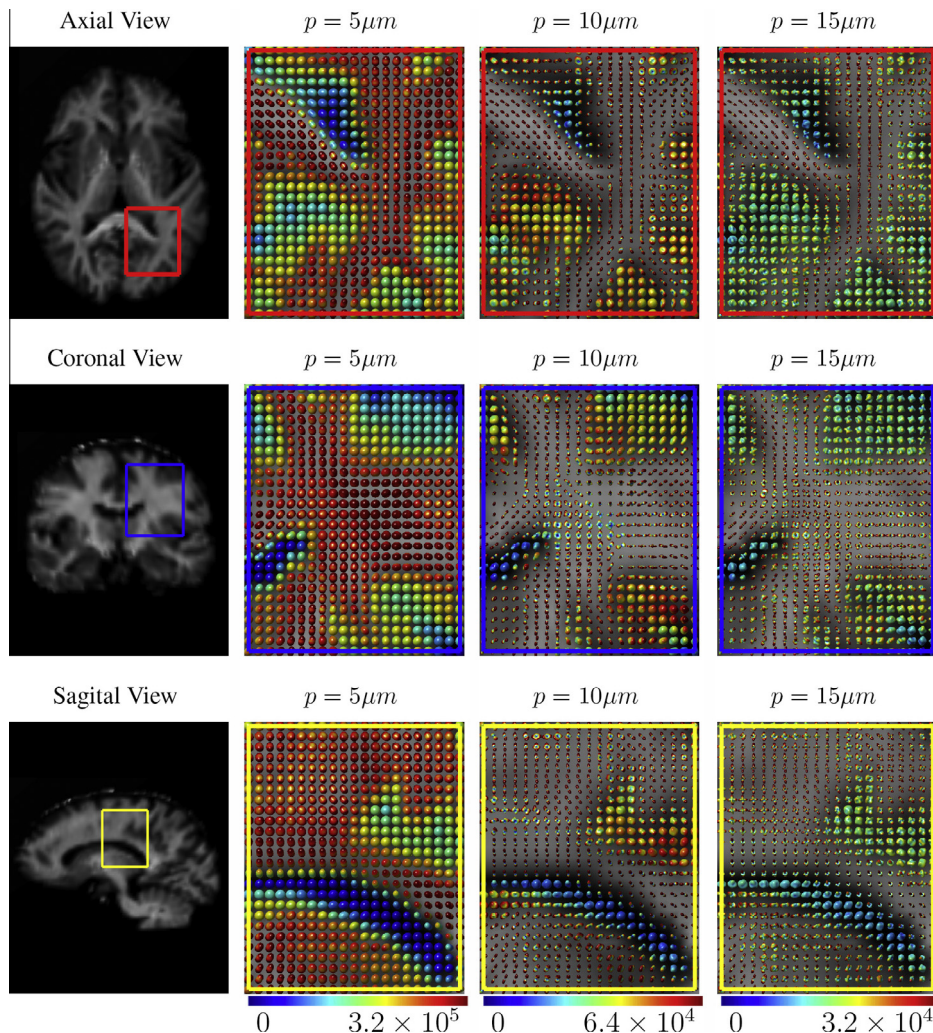


**Fig. 3.** The estimated HYDI atlas in the ensemble average propagator (EAP) space. The first column shows the atlas in terms of the zero displacement probability (Po). The second to fourth columns respectively illustrate the fiber orientation profiles of the atlas at three given radii ( $p = 5, 10, 15$   $\mu\text{m}$ ) in the EAP space. The color indicates the values of EAP. (For interpretation of the references to color in this figure legend, the reader is referred to the web version of this article.)

atlas zero-displacement probability ( $P_0$ ) (Assaf et al., 2000), mean squared displacement (MSD) (Wu and Alexander, 2007), and generalized fractional anisotropy (GFA) under three different radii

(Tuch, 2004). These figures visually illustrate that the estimated atlas has the anatomical details of the brain white matter, particularly in the region near the cortex.

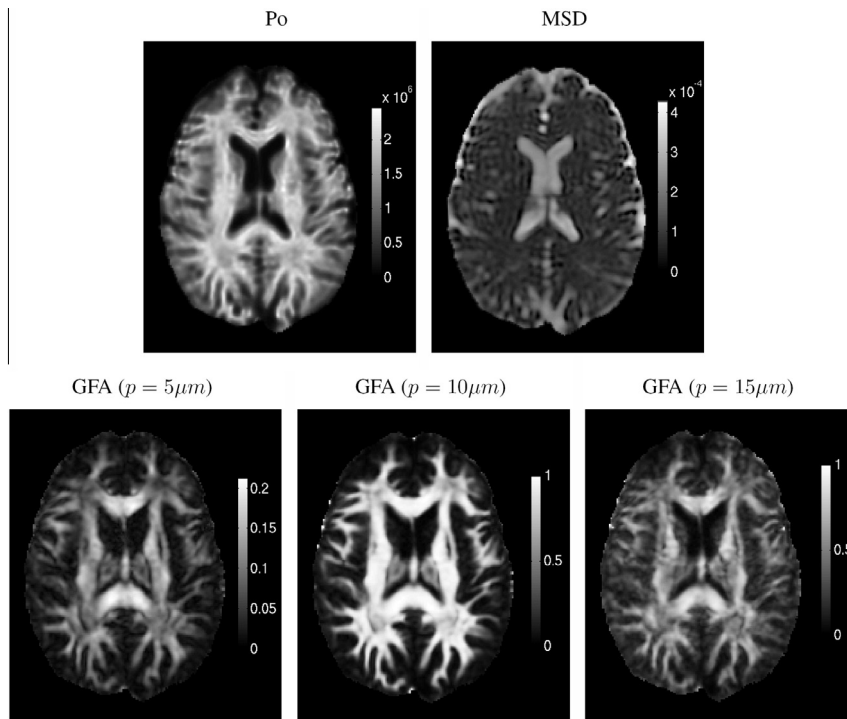


**Fig. 4.** Illustration of the estimated atlas on the zero-displacement probability ( $P_0$ ), mean squared displacement (MSD), and generalized fractional anisotropy (GFA) at three given radii ( $p = 5, 10, 15 \mu\text{m}$ ) of the ensemble average propagator (EAP) space.

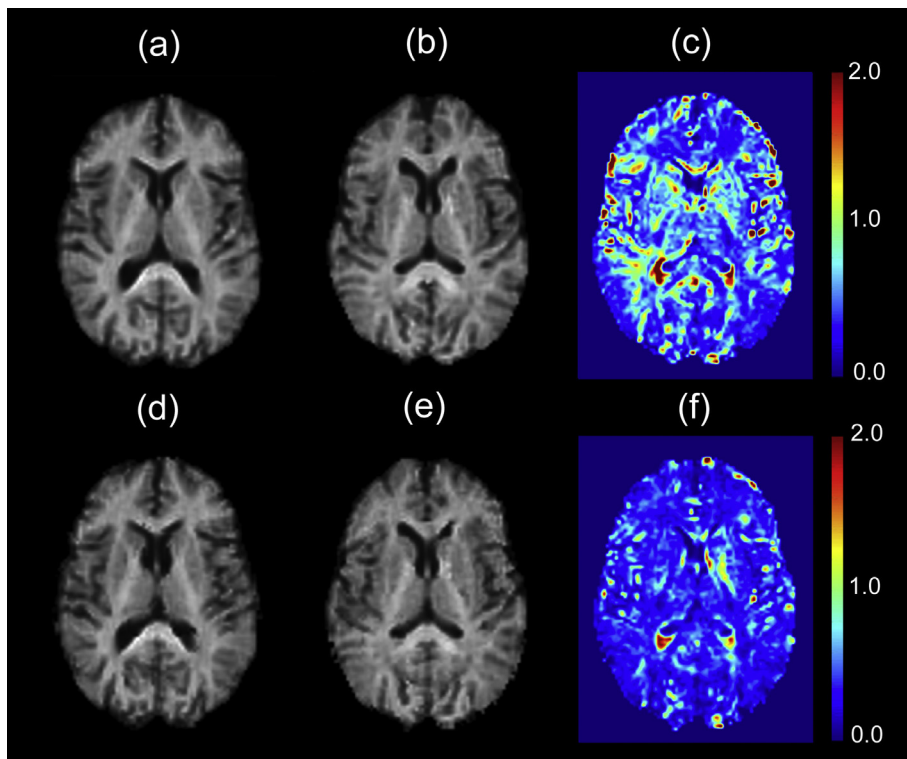


**Fig. 5.** Influences of the hyperatlas on the estimated atlas. Panels (a, b) show the zero-displacement probability images of two HYDI subjects used as the hyperatlas in the Bayesian atlas estimation. Panels (d, e) show the atlases generated respectively based on hyperatlases in panels (a, b). Panel (c) shows the symmetrized Kullback–Leibler (sKL) divergence between the diffusion probability density functions of the two hyperatlases on (a, b), while panel (f) shows that between the estimated atlases on panels (d, e).

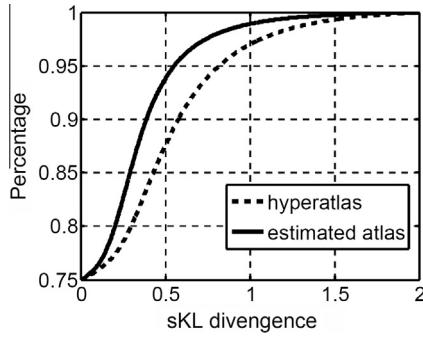


**Fig. 6.** The cumulative distributions of the sKL divergence between the two hyperatlases (Fig. 5(a and b)) and between the two estimated atlases (Fig. 5(d and e)) are respectively shown in the dashed and solid lines.

Finally, we study the effects of the hyperatlas choice on the estimated atlas. In the Bayesian modeling for the HYDI atlas generation presented here, the hyperatlas is assumed to be known and fixed. In addition, the hyperatlas is used as the initialization for the atlas in the EM algorithm. Therefore, there is possibility that the anatomy of the estimated atlas could be influenced by the choice of the hyperatlas. We now demonstrate this influence on the estimated atlas due to the hyperatlas.

We repeated the atlas estimation procedure when two different HYDI subjects, shown in Fig. 5(a and b), were respectively selected as the hyperatlas. Fig. 5(d and e) shows the estimated HYDI atlases obtained from the hyperatlases shown in Fig. 5(a and b), respectively. To evaluate the similarity between the two hyperatlases and estimated atlases, we first computed the diffusion probability density functions (PDFs) of water molecules, i.e., the ensemble average propagator (EAP), using Fourier transform (Hosseinbor

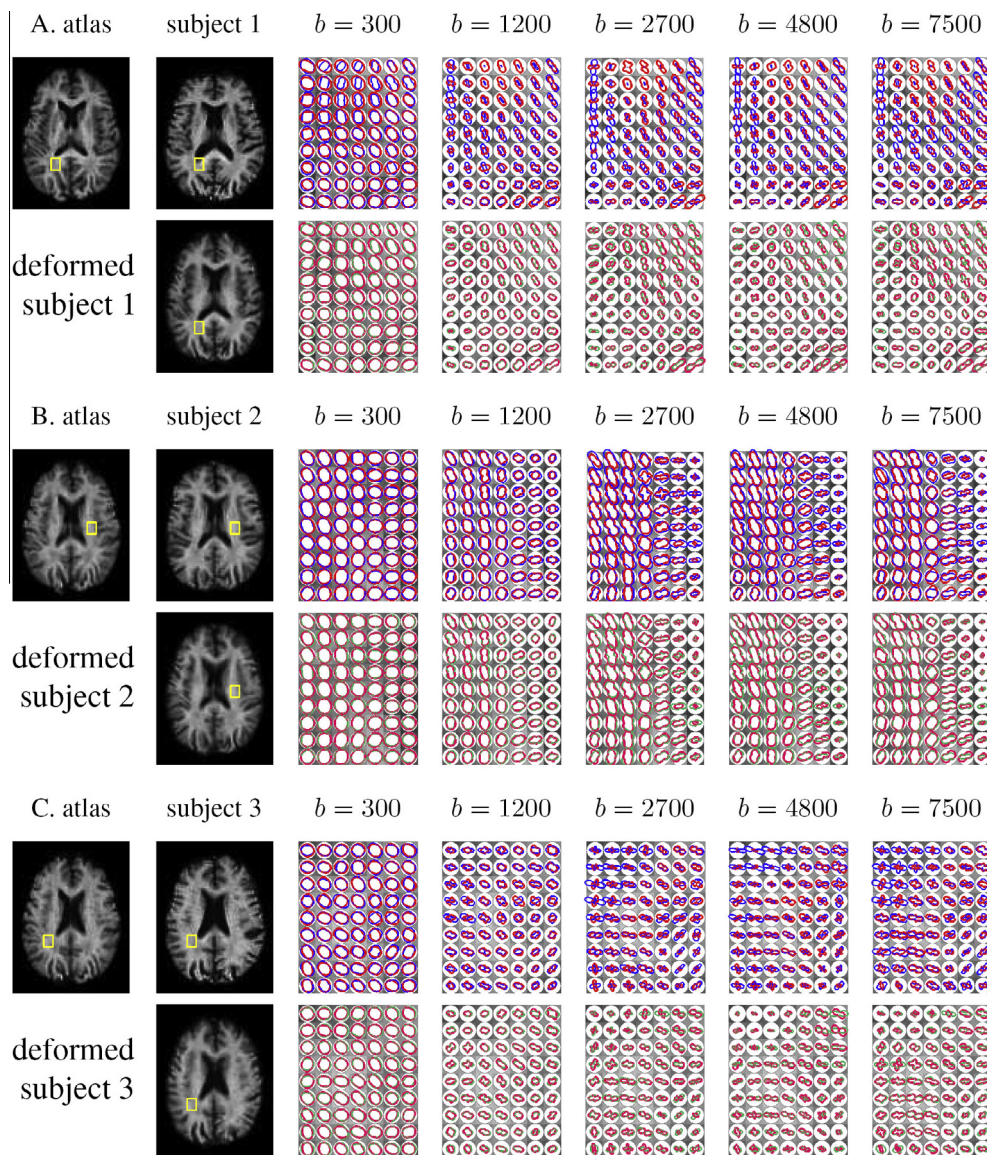


**Fig. 7.** Illustration of the LDDMM-HYDI mapping results. The first row of panels (A–C) illustrates the atlas image, subject image, the diffusion profiles at individual shells with  $b = 300, 1200, 2700, 4800,$  and  $7500 \text{ s/mm}^2$  in the  $q$ -space, respectively. The second row of panels (A–C) illustrates the deformed subject image in the atlas space after the LDDMM-HYDI mapping, the diffusion profiles at individual shells with  $b = 300, 1200, 2700, 4800,$  and  $7500 \text{ s/mm}^2$  in the  $q$ -space, respectively. Red, blue, and green contours in the last five columns respectively illustrate the diffusion profiles of the atlas, subject, and deformed subject in atlas space. The closer the green contour to the red contour, the better the alignment. Note that the profile of diffusion weighted signals is shown in this figure. It is orthogonal to the fiber orientation. (For interpretation of the references to color in this figure legend, the reader is referred to the web version of this article.)

et al., 2013) and then calculated the symmetrized Kullback–Leibler (sKL) divergence between the PDFs (Chiang et al., 2008) at individual voxels. As seen in Fig. 5(c), the sKL divergence is large between the PDFs of the two hyperatlases even in the corpus callosum and external capsule. Nevertheless, Fig. 5(f) shows the sKL divergence between the PDFs of the two estimated atlases and illustrates a reduction in the sKL divergence compared to that in Fig. 5(c). A two-sample Kolmogorov–Smirnov test reveals that the cumulative distribution of the sKL divergence as shown in Fig. 6 between the two estimated atlases (Fig. 5(d and e)) is significantly greater than that between the two hyperatlases (Fig. 5(a and b)) ( $p < 0.001$ ), which indicates that more voxels with small sKL divergence between the two estimated atlases when compared to those between the two hyperatlases. This result suggests the improved similarity between the two estimated atlases when compared to that between the two hyperatlases.

## 5.2. HYDI mapping

Given the atlas generated in Section 5.1, we mapped the 36 subjects into the atlas space using LDDMM-HYDI with  $\sigma_V = 10$ . To evaluate the mapping results, we first illustrate the mapping results of HYDI datasets using LDDMM-HYDI and then evaluate the influence of the reorientation on the optimization of the diffeomorphic transformation. Finally, we compare the mapping accuracy of LDDMM-HYDI with that of an existing diffeomorphic registration method for DTI (Cao et al., 2005) that was adapted to multiple tensors generated from each shell of the  $q$ -space.

Fig. 7 shows the LDDMM-HYDI mapping results of three subjects. The last five columns respectively illustrate the geometric shapes of the diffusion signals at five shells of the  $q$ -space in the brain regions with crossing fibers. Red, blue, and green contours respectively represent the shape of the diffusion signals from the atlas, subject, and deformed subjects. Visually, the diffusion profiles at each shell can be matched well after the mapping.

We next evaluated the mapping accuracy of the LDDMM-HYDI algorithms with and without the computation of Term (B) in Eq. (11) during the optimization, where Term (B) seeks the diffeomorphic transformation such that the local diffusion profiles of the atlas and subject's HYDIs can be aligned. We demonstrate the importance of Term (B) in the optimization of the HYDI registration even though it is often neglected in existing DWI-based registration algorithms (e.g., Dhollander et al., 2010, 2011). For this, we first computed the diffusion probability density functions (PDFs) of water molecules, i.e., the ensemble average propagator (EAP), using Fourier transform Hosseinbor et al. (2013). Then, we calculated the symmetrized Kullback–Leibler (sKL) divergence between the deformed subject and atlas PDFs (Chiang et al., 2008) in major white matter tracts. The smaller sKL metric indicates the better alignment between the deformed subject and atlas HYDIs. The major white matter tracts evaluated in this study include corpus callosum (CC), corticospinal tract (CST), internal capsule (IC), corona radiata (CR), external capsule (EC), cingulum (CG), superior longitudinal fasciculus (SLF), and inferior fronto-occipital fasciculus (IFO). Table 2 lists the values of the mean and standard deviation of the sKL metric for each major white matter tract among 36 subjects when the LDDMM-HYDI algorithms with and without the Term (B) computation were respectively employed. Pairwise Student  $t$ -tests suggest that the LDDMM-HYDI algorithm with the explicit orientation optimization (Term (B) computation) significantly improves the alignment in the major white matter tracts when compared to that without the explicit orientation optimization (Student's  $t$ -tests:  $p < 0.05$  for all tracts).

Last, we compared the mapping accuracy of LDDMM-HYDI with that of an existing diffeomorphic registration method for DTI (Cao et al., 2005) that was adapted to multiple tensors generated from

each shell of the  $q$ -space. The LDDMM multi-tensor mapping is superior to the existing approach that aligns DWIs on multiple shells of the  $q$ -space based on the generalized fractional anisotropy (GFA) images computed from each shell (Dhollander et al., 2011). In this experiment, we first computed three diffusion tensors derived from the diffusion weighted images at  $b = 1200$ , 2700, and 4800  $s/mm^2$ . We then employed the LDDMM multi-tensor mapping algorithm to simultaneously align the three tensor images of a subject to those of the atlas. This multi-tensor mapping algorithm (LDDMM multi-tensor) was implemented under the same LDDMM framework as one for the LDDMM-HYDI mapping algorithm presented in this paper. Hence, we chose the same parameter,  $\sigma_V = 5$ , to control the smoothness of the deformation. The transformation obtained from this multi-tensor diffeomorphic mapping was finally applied to the DWI signals based on reorientation scheme given in Eq. (6). Table 3 lists the squared difference in the diffusion signals between the atlas and deformed subjects

**Table 2**

Table lists the mean and standard deviation values of the symmetrized Kullback–Leibler (sKL) divergence of the diffusion probability density functions (PDFs) between the deformed subject and atlas HYDIs in each major white matter tract. The second and third columns show the results obtained from the LDDMM-HYDI without and with the Term (B) computation. *Abbreviations:* CC–corpus callosum; CST–corticospinal tract; IC– internal capsule; CR–corona radiata; EC–external capsule, CG–cingulum, SLF–superior longitudinal fasciculus, and IFO–inferior fronto-occipital fasciculus.

	LDDMM-HYDI without Term (B)	LDDMM-HYDI with Term (B)
CST	0.477(0.084)	0.434(0.066)
CC	0.369(0.046)	0.346(0.046)
IC	0.387(0.045)	0.377(0.044)
CR	0.289(0.038)	0.282(0.038)
EC	0.327(0.032)	0.322(0.032)
CG	0.417(0.048)	0.406(0.048)
SLF	0.341(0.059)	0.327(0.060)
IFO	0.374(0.037)	0.366(0.037)

**Table 3**

Comparison of the mapping accuracy between LDDMM-HYDI and LDDMM multi-tensor. The first column lists the  $b$ -value ( $s/mm^2$ ) of each shell. The second and third columns list the squared difference in the diffusion signals of the deformed subjects and the atlas after the LDDMM multi-tensor and LDDMM-HYDI mapping, respectively. Mean and standard deviation are given.

	LDDMM multi-tensor ( $\times 10^4$ )	LDDMM-HYDI ( $\times 10^4$ )
$b = 300$	3.958(0.405)	3.236(0.394)
$b = 1200$	2.106(0.162)	1.928(0.183)
$b = 2700$	1.084(0.075)	0.827(0.061)
$b = 4800$	0.680(0.047)	0.462(0.035)
$b = 7500$	0.375(0.030)	0.248(0.024)

**Table 4**

Table lists the mean and standard deviation values of the symmetrized Kullback–Leibler (sKL) divergence of the diffusion probability density functions (PDFs) between the deformed subject and atlas HYDIs in each major white matter tract. The second and third columns show the results obtained from the LDDMM multi-tensor and LDDMM-HYDI mapping. *Abbreviations:* CC–corpus callosum; CST–corticospinal tract; IC– internal capsule; CR–corona radiata; EC–external capsule, CG–cingulum, SLF–superior longitudinal fasciculus, and IFO–inferior fronto-occipital fasciculus.

	LDDMM multi-tensor	LDDMM-HYDI
CST	0.983(0.234)	0.434(0.066)
CC	0.657(0.062)	0.346(0.046)
IC	0.642(0.066)	0.377(0.044)
CR	0.478(0.052)	0.282(0.038)
EC	0.411(0.048)	0.322(0.032)
CG	0.654(0.055)	0.406(0.048)
SLF	0.617(0.075)	0.327(0.060)
IFO	0.422(0.044)	0.366(0.037)

after the LDDMM multi-tensor and LDDMM-HYDI mapping. Pairwise Student  $t$ -tests suggested the significant improvement in the alignment of DWIs using LDDMM-HYDI against LDDMM multi-tensor ( $p < 0.05$ ) at every shell of the  $q$ -space. Furthermore, we computed the sKL divergence between the PDFs of the atlas and the subjects deformed using the LDDMM multi-tensor and LDDMM-HYDI mapping for major white matter tracts. Table 4 lists the values of the mean and standard deviation of the sKL metric for each major white matter tract among 36 subjects when the LDDMM multi-tensor and LDDMM-HYDI algorithms were respectively employed. Pairwise Student  $t$ -tests suggest that the LDDMM-HYDI algorithm significantly improves the alignment in the major white matter tracts when compared to that obtained using LDDMM multi-tensor mapping (Student's  $t$ -tests:  $p < 0.05$  for all tracts).

## 6. Conclusion

In conclusion, we proposed the LDDMM-HYDI variational problem and the Bayesian atlas estimation model based on the BFOR signal basis representation of DWIs. We derived the gradient of this variational problem with the explicit computation of the mDWI reorientation and provided a numeric algorithm without a need of the discretization in the  $q$ -space. Comparing with our existing work (Du et al., 2013), we further derived the EM algorithm for the estimation of the atlas in the Bayesian framework. Moreover, we provided the extensive evaluation on the mapping accuracy based on a new dataset of 36 healthy adults and compared LDDMM-HYDI with that of the diffeomorphic mapping based on diffusion tensors. Our results showed that (1) the atlas generated contains anatomical details of the white matter anatomy; (2) the explicit orientation optimization is necessary as it improves the alignment of the diffusion profiles of HYDI datasets; and (3) the comparison with the multi-tensor based diffeomorphic metric mapping suggests the importance for incorporating the full information of HYDI for the mDWI registration.

In this paper, our study was not able to examine the mapping accuracy using HARDI mapping approaches (e.g., Du et al. (2012), Raffelt et al. (2012)) as the imaging acquisition in each shell in our study is not sufficient to reconstruct the HARDI model. Moreover, we did not compare the performance of the LDDMM-HYDI mapping with that of the existing HYDI mapping approach (Dhollander et al., 2011). First of all, the influence of the reorientation on the optimization of the diffeomorphic transformation is shown to be crucial. The mapping algorithm in Dhollander et al. (2011) takes GFA images obtained from each shell of the  $q$ -space and estimates the deformation using a multi-channel diffeomorphic image mapping algorithm without the explicit computation of the reorientation during the optimization of the mapping algorithm. Second, we examined the mapping using multiple tensors generated from each shell in the  $q$ -space, which is superior than that using GFA images obtained from each shell in the  $q$ -space as given in Dhollander et al. (2011). Hence, we expect that the conclusion that LDDMM-HYDI outperforms LDDMM multi-tensor can be generalized to the existing HYDI mapping approach (Dhollander et al., 2011).

## Acknowledgments

The work was supported by the Young Investigator Award at the National University of Singapore (NUSYIA FY10 P07), the National University of Singapore MOE AcRF Tier 1, Singapore Ministry of Education Academic Research Fund Tier 2 (MOE2012-T2-2-130), and NIH grants (MH84051, HD003352, AG037639, and AG033514).

## Appendix A. Derive $\sigma^{2\text{new}}$ from the $Q$ -function

We update  $\sigma^2$  when  $m_0$  is fixed and  $\phi_1^{(i)}, i = 1, 2, \dots, n$  are known. Hence,

$$\begin{aligned} Q(m_0, \sigma^2 | m_0^{\text{old}}, \sigma^{2\text{old}}) &= \langle m_0, k_V m_0 \rangle_2 + \sum_{i=1}^n E \left[ \int_{\mathbf{x} \in \Omega} \left\{ \frac{1}{\sigma^2} \left\| (\mathbf{M}(R_{\mathbf{x}}) \mathbf{c}^{\text{atlas}}) \right. \right. \right. \\ &\quad \left. \left. \left. \circ (\phi_1^{(i)})^{-1}(\mathbf{x}) - \mathbf{c}^{(i)}(\mathbf{x}) \right\|^2 + \log \sigma^2 \right\} d\mathbf{x} \right] \\ &= \langle m_0, k_V m_0 \rangle_2 + \sum_{i=1}^n \int_{\mathbf{x} \in \Omega} \left\{ \frac{1}{\sigma^2} \left\| (\mathbf{M}(R_{\mathbf{x}}) \mathbf{c}^{\text{atlas}}) \right. \right. \\ &\quad \left. \left. \left. \circ (\phi_1^{(i)})^{-1}(\mathbf{x}) - \mathbf{c}^{(i)}(\mathbf{x}) \right\|^2 + \log \sigma^2 \right\} d\mathbf{x}. \end{aligned}$$

We now take the derivative of  $Q$  with respect to  $\sigma^2$ .

$$\frac{dQ}{d\sigma^2} = \sum_{i=1}^n \int_{\mathbf{x} \in \Omega} \left\{ -\frac{1}{\sigma^4} \left\| (\mathbf{M}(R_{\mathbf{x}}) \mathbf{c}^{\text{atlas}}) \circ (\phi_1^{(i)})^{-1}(\mathbf{x}) - \mathbf{c}^{(i)}(\mathbf{x}) \right\|^2 + \frac{1}{\sigma^2} \right\} d\mathbf{x}.$$

We set  $\frac{dQ}{d\sigma^2} = 0$  and thus have

$$\sigma^{2\text{new}} = \frac{1}{n} \frac{1}{n_V} \sum_{i=1}^n \int_{\mathbf{x} \in \Omega} \left\| (\mathbf{M}(R_{\mathbf{x}}) \mathbf{c}^{\text{atlas}}) \circ (\phi_1^{(i)})^{-1}(\mathbf{x}) - \mathbf{c}^{(i)}(\mathbf{x}) \right\|^2 d\mathbf{x},$$

where  $n_V$  is the number of voxels in  $\Omega$ .

## References

- Alexander, D., Pierpaoli, C., Basser, P., Gee, J., 2001. Spatial transformation of diffusion tensor magnetic resonance images. *IEEE Trans. Med. Imaging* 20, 1131–1139.
- Assaf, Y., Mayk, A., Cohen, Y., 2000. Displacement imaging of spinal cord using  $q$ -space diffusion-weighted MRI. *Magn. Reson. Med.* 44, 713722.
- Assemal, H.E., Tschumperlin, D., Brun, L., 2009. Efficient and robust computation of pdf features from diffusion mr signal. *Med. Image Anal.* 13, 715–729.
- Beg, M.F., Miller, M.L., Trounev, A., Younes, L., 2005. Computing large deformation metric mappings via geodesic flows of diffeomorphisms. *Int. J. Comput. Vision* 61, 139–157.
- Cao, Y., Miller, M., Winslow, R., Younes, L., 2005. Large deformation diffeomorphic metric mapping of vector fields. *IEEE Trans. Med. Imaging* 24, 1216–1230.
- Cetingul, H., Afsari, B., Vidal, R., 2012. An algebraic solution to rotation recovery in hardi from correspondences of orientation distribution functions. In: 2012 9th IEEE International Symposium on Biomedical Imaging (ISBI), pp. 38–41.
- Cheng, J., Ghosh, A., Jiang, T., Deriche, R., 2010. Model-free and analytical eap reconstruction via spherical polar fourier diffusion MRI. In: Proceedings of the 13th International Conference on Medical Image Computing and Computer-Assisted Intervention, pp. 590–597.
- Chiang, M.C., Leow, A., Klunder, A., Dutton, R., Barysheva, M., Rose, S., McMahon, K., de Zubicaray, G., Toga, A., Thompson, P., 2008. Fluid registration of diffusion tensor images using information theory. *IEEE Trans. Med. Imaging* 27, 442–456.
- Descoteaux, M., Angelino, E., Fitzgibbons, S., Deriche, R., 2006. Apparent diffusion coefficients from high angular resolution diffusion imaging: estimation and applications. *Magn. Reson. Med.* 56, 395–410.
- Descoteaux, M., Deriche, R., Bihan, D.L., Mangin, J.F., Poupon, C., 2011. Multiple  $q$ -shell diffusion propagator imaging. *Med. Image Anal.* 15, 603–621.
- Dhollander, T., Van Hecke, W., Maes, F., Sunaert, S., Suetens, P., 2010. Spatial transformations of high angular resolution diffusion imaging data in  $Q$ -space. In: MICCAI CDMRI Workshop, pp. 73–83.
- Dhollander, T., Veraart, J., Van Hecke, W., Maes, F., Sunaert, S., Sijbers, J., Suetens, P., 2011. Feasibility and advantages of diffusion weighted imaging atlas construction in  $q$ -space. In: Proceedings of the 14th International Conference on Medical Image Computing and Computer-Assisted Intervention – Volume Part II, pp. 166–173.
- Dorst, L., 2005. First order error propagation of the procrustes method for 3d attitude estimation. *IEEE Trans. Pattern Anal. Mach. Intell.* 27, 221–229.
- Du, J., Goh, A., Qiu, A., 2012. Diffeomorphic metric mapping of high angular resolution diffusion imaging based on riemannian structure of orientation distribution functions. *IEEE Trans. Med. Imaging* 31, 1021–1033.
- Du, J., Hosseinbor, A.P., Chung, M.K., Bendlin, B.B., Suryawanshi, G., Alexander, A.L., Qiu, A., 2013. Diffeomorphic metric mapping of hybrid diffusion imaging based on BFOR signal basis. In: Information Processing in Medical Imaging.
- Du, J., Younes, L., Qiu, A., 2011. Whole brain diffeomorphic metric mapping via integration of sulcal and gyral curves, cortical surfaces, and images. *NeuroImage* 56, 162–173.
- Edmonds, A.R., 1996. *Angular Momentum in Quantum Mechanics*. Princeton University Press.
- Essen, D.C.V., Smith, S.M., Barch, D.M., Behrens, T.E., Yacoub, E., Ugurbil, K., 2013. The wu-minn human connectome project: an overview. *NeuroImage* 80, 62–79.

- Geng, X., Ross, T.J., Gu, H., Shin, W., Zhan, W., Chao, Y.P., Lin, C.P., Schuff, N., Yang, Y., 2011. Diffeomorphic image registration of diffusion mri using spherical harmonics. *IEEE Trans. Med. Imaging* 30, 747–758. <http://dx.doi.org/10.1109/TMI.2010.2095027>.
- Hosseinbor, A.P., Chung, M.K., Wu, Y.C., Alexander, A.L., 2013. Bessel fourier orientation reconstruction (bfor): an analytical diffusion propagator reconstruction for hybrid diffusion imaging and computation of q-space indices. *NeuroImage* 64, 650–670.
- Hsu, Y.C., Hsu, C.H., Tseng, W.Y.I., 2012. A large deformation diffeomorphic metric mapping solution for diffusion spectrum imaging datasets. *NeuroImage* 63, 818–834.
- Ma, J., Miller, M.I., Trounev, A., Younes, L., 2008. Bayesian template estimation in computational anatomy. *NeuroImage* 42, 252–261.
- Ozarslan, E., Koay, C., Shepherd, T.M., Blackb, S.J., Basser, P.J., 2008. Simple harmonic oscillator based reconstruction and estimation for three-dimensional q-space MRI. In: *Proc. Intl. Soc. Mag. Reson. Med.*
- Qiu, A., Brown, T., Fischl, B., Ma, J., Miller, M.I., 2010. Atlas generation for subcortical and ventricular structures with its applications in shape analysis. *IEEE Trans. Image Process.* 19, 1539–1547.
- Raffelt, D., Tournier, J.D., Crozier, S., Connelly, A., Salvado, O., 2012. Reorientation of fiber orientation distributions using apodized point spread functions. *Magn. Reson. Med.* 67, 844–855.
- Raffelt, D., Tournier, J.D., Fripp, J., Crozier, S., Connelly, A., Salvado, O., 2011. Symmetric diffeomorphic registration of fibre orientation distributions. *NeuroImage* 56, 1171–1180.
- Tuch, D.S., 2004. Q-ball imaging. *Magn. Reson. Med.* 52, 1358–1372.
- Wedeen, V.J., Hagmann, P., Tseng, W.Y.I., Reese, T.G., Weisskoff, R.M., 2005. Mapping complex tissue architecture with diffusion spectrum magnetic resonance imaging. *Magn. Reson. Med.* 54, 1377–1386.
- Wu, Y.C., Alexander, A.L., 2007. Hybrid diffusion imaging. *NeuroImage* 36, 617–629.
- Yap, P.T., Shen, D., 2012. Spatial transformation of dwi data using non-negative sparse representation. *IEEE Trans. Med. Imaging* 31, 2035–2049. <http://dx.doi.org/10.1109/TMI.2012.2204766>.
- Yeo, B., Vercauteren, T., Fillard, P., Peyrat, J.M., Pennec, X., Golland, P., Ayache, N., Clatz, O., 2009. Dt-refind: diffusion tensor registration with exact finite-strain differential. *IEEE Trans. Med. Imaging* 28, 1914–1928.
- Zhang, P., Niethammer, M., Shen, D., Yap, P.T., 2012. Large deformation diffeomorphic registration of diffusion-weighted images. In: *MICCAI*.